Antigen affinity discrimination is an intrinsic function of the B cell receptor

Wanli Liu,[1] Tobias Meckel,[2] Pavel Tolar,[3] Hae Won Sohn,[1] and Susan K. Pierce[1]

[1]Laboratory of Immunogenetics, National Institute of Allergy and Infectious Diseases, National Institutes of Health, Rockville, MD 20852
[2]Department of Biology Membrane Biophysics, Darmstadt University of Technology, 64287 Darmstadt, Germany
[3]National Institute for Medical Research, London NW7 1AA, England, UK

Antibody affinity maturation, a hallmark of adaptive immune responses, results from the selection of B cells expressing somatically hypermutated B cell receptors (BCRs) with increased affinity for antigens. Despite the central role of affinity maturation in antibody responses, the molecular mechanisms by which the increased affinity of a B cell for antigen is translated into a selective advantage for that B cell in immune responses is incompletely understood. We use high resolution live-cell imaging to provide evidence that the earliest BCR-intrinsic events that follow within seconds of BCR–antigen binding are highly sensitive to the affinity of the BCR for antigen. High affinity BCRs readily form oligomers and the resulting microclusters grow rapidly, resulting in enhanced recruitment of Syk kinase and calcium fluxes. Thus, B cells are able to read the affinity of antigen by BCR-intrinsic mechanisms during the earliest phases of BCR clustering, leading to the initiation of B cell responses.

CORRESPONDENCE
Susan K. Pierce:
spierce@nih.gov

Abbreviations used: 2D, two dimensional; CPD, cumulative probability distribution; FI, fluorescence intensity; FRET, fluorescence resonance energy transfer; FWHM, full width at half-maximum peak height; GC, germinal center; IS, immunological synapse; mIg, membrane Ig; MSD, mean square displacement; NIP, 4-hydroxy-3-iodo-5-nitrophenyl; NP, 4-hydroxy-3-nitrophenyl; pNP, 4-nitrophenylacetic acid; pSyk, phosphorylated Syk; TIRF, total internal reflection fluorescence; TIRFM, TIRF microscopy.

Affinity maturation, the increase in the affinity of antigen-specific antibodies during the course of immune responses, is a central, unique feature of humoral immunity. Memory is encoded, in part, in long-lived memory B cells that are the differentiated product of germinal center (GC) reactions in which B cells undergo somatic hypermutation and antigen selection (McHeyzer-Williams and McHeyzer-Williams, 2005). B cells expressing high affinity BCRs are favored in the antigen selection process, although the molecular basis of the advantage of high affinity BCRs in B cell selection is not completely understood. Studies in transgenic mouse models in vivo provided evidence that selection works at the level of competition between B cell clones (Takahashi et al., 1998; Dal Porto et al., 2002; Shih et al., 2002a,b; Brink et al., 2008). Transgenic mouse strains expressing BCRs that differed 40-fold in their affinity for the hapten 4-hydroxy-3-nitrophenyl (NP) showed only a 2-fold difference in the level of antibody produced in response to immunization with a T cell–independent NP-containing antigen (Shih et al., 2002b). Similarly, these two strains of mice showed comparable levels of NP-specific antibodies and GC formation in response to immunization with a T cell–dependent NP-containing antigen (Shih et al., 2002a). Collectively, these studies suggested that there are few differences in the intrinsic ability of high and low affinity BCRs to activate B cells. However, in adoptive transfer experiments using mixtures of high and low affinity B cells, only high affinity B cells responded to T cell–independent antigen and only high affinity B cells accumulated in GCs after immunization with a T cell–dependent antigen. Evidence was also provided that stringent selection for high affinity B cell clones was imposed in the early stages of the B cell response (pre-GC; Shih et al., 2002a,b). Similar results were obtained in separate studies analyzing the response of B cells with differing affinities for either NP (Takahashi et al., 1998; Dal Porto et al., 2002) or hen egg lysozyme (Paus et al., 2006; Phan et al., 2006). Collectively, these results suggested that the selective advantage of high affinity BCRs is at the level of a B cell clone's ability to compete for antigen, survival niches, T cell

The Rockefeller University Press $30.00
J. Exp. Med. Vol. 207 No. 5 1095-1111
www.jem.org/cgi/doi/10.1084/jem.20092123

The Journal of Experimental Medicine

help, or other limiting factors. In contrast, studies of the responses of transgenic B cells specific for the MHC class I molecule H-2K^K to high versus low affinity H-2K^K–derived phage-displayed peptides provided evidence that BCRs differentially signaled in response to antigens of different affinities (Kouskoff et al., 1998). The results showed that the ability of the soluble phage antigen to stimulate certain early signaling responses was highly affinity dependent, whereas others were not. At present, the molecular link between antigen binding to high affinity BCRs and increased clonal competitiveness in selection in vivo or differential signaling in vitro are not known.

The advent of high resolution imaging in living cells and its application to the study of antigen-induced BCR signaling is providing an increasingly detailed view of the earliest events in the initiation of BCR signaling that follow antigen binding (Carrasco and Batista, 2006; Harwood and Batista, 2008; Tolar et al., 2008, 2009b; Batista and Harwood, 2009; Tolar and Pierce, 2010). Recent studies have focused on B cells recognizing antigen on the surface of APCs, a context that intervital imaging suggests may be highly relevant to B cell activation in vivo (Qi et al., 2006; Carrasco and Batista, 2007; Junt et al., 2007; Pape et al., 2007; Phan et al., 2007). Fleire et al. (2006) provided the first detailed description of the molecular events that follow the B cell's encounter with antigen-containing fluid planar lipid bilayers in vitro as a surrogate for APCs. They observed that BCRs clustered almost exclusively in the initial points of contact between the B cells and the antigen-containing lipid bilayers. Signaling from the BCR clusters induced the B cells to dramatically spread over the bilayer. As the B cells spread, additional BCR–antigen microclusters formed in the peripheral lamellopodia of the cell and then moved to the center of the contact area by an actin-dependent mechanism. The observation that BCRs formed microclusters in the first steps of immunological synapse (IS) formation suggests that the clusters are the B cell's elementary signaling unit. After maximal spreading, the B cells contracted to form an ordered IS. This remarkably dynamic process was shown to help B cells discriminate between high and low affinity antigens, as the more antigens engaged, the stronger the spreading response, resulting in the engagement of more antigens and providing a feedback loop that amplifies the difference in affinity-dependent antigen collection. These results indicated that in addition to a role of BCR affinity in competition between B cell clones, high affinity BCRs provided a B cell–intrinsic advantage in B cell responses.

Our recent studies focused on the initiation of the formation of signaling-active BCR microclusters at the points of initial contact between the B cell and the antigen-containing bilayer that precede the triggering of the active spreading and contraction response and the formation of an IS. Using a combination of fluorescence resonance energy transfer (FRET) microscopy and high resolution single-molecule total internal reflection fluorescence (TIRF) imaging, we recently provided evidence for an ordered series of BCR-intrinsic events in the initiation of BCR signaling that involved conformational changes in both the ectodomain and the cytoplasmic domains of the antigen-engaged BCRs (Tolar et al., 2008, 2009a,b). We observed that the binding of antigen at the initial sites of contact between B cells and antigen-containing fluid bilayers resulted in the formation of BCR microclusters in which immobile BCR oligomers assembled in a BCR-intrinsic process that did not require a signaling-active BCR (Tolar et al., 2009a). The formation of oligomers depended on the Cμ4 domain of the BCR's membrane Ig (mIg); BCRs that lacked a Cμ4 domain failed to form oligomers and signal, and conversely, BCRs that contained mIg's with only Cμ4 ectodomains oligomerized spontaneously and activated B cells (Tolar et al., 2009a). These results supported a "conformation-induced oligomerization" model for the initiation of B cell signaling, as recently described (Tolar and Pierce, 2010). We also provided evidence that in the development of signaling-active BCR microclusters, the BCRs undergo a change in the cytoplasmic domains from a "closed" to an "open" form that occurs simultaneously with the phosphorylation of the BCR's immunoreceptor tyrosine-based activation motifs (Tolar et al., 2005; Sohn et al., 2008). Collectively, these studies suggest that the initiation of BCR signaling involves a series of dynamic yet ordered molecular events.

In this paper, we investigate the impact of the BCRs' affinity for antigen on these early events in the initiation of BCR signaling and provide evidence that these BCR-intrinsic events are highly affinity dependent. High affinity compared with low affinity BCRs form increased numbers of immobile BCR oligomers, show increased rates of cluster growth, and transition from closed to open forms, resulting in enhanced recruitment of Syk and calcium fluxes. Thus, B cells expressing high affinity BCRs have an intrinsic advantage over low affinity BCRs in the initiation of BCR oligomerization events that lead to the triggering of signaling cascades. These results place affinity discrimination at the earliest steps in the initiation of BCR responses. We suggest that these affinity-sensitive BCR-intrinsic events in the initiation of signaling may be amplified by B cell spreading and contraction responses, ultimately leading to enhanced clonal competition in affinity maturation.

RESULTS

High affinity BCRs show an enhanced ability to oligomerize

We recently provided evidence using single-molecule imaging techniques that the formation of immobile BCR oligomers was one of the earliest antigen-induced, BCR-intrinsic events leading to BCR signaling (Tolar et al., 2009a). To determine if the formation of immobile BCR oligomers was influenced by the affinity of the BCR for antigen, we tracked single BCRs by TIRF microscopy (TIRFM) on J558L cells expressing BCRs with either high or low affinity for the hapten 4-hydroxy-3-iodo-5-nitrophenyl (NIP) as they engaged NIP-containing fluid lipid bilayers.

Our previous studies provided evidence that BCR oligomerization did not require physical cross-linking of the BCR by multivalent antigens when B cells encountered antigens

on a fluid lipid bilayer (Tolar et al., 2009a). Consequently, in the studies described in this paper, we used as antigen a previously described monovalent NIP1 hapten conjugated to a 31-aa peptide containing 12 His residues (NIP1-His12), allowing the peptide to be attached to nickel-containing lipid bilayers. The use of a monovalent antigen in a fluid bilayer that does not have the capacity to physically cross-link BCRs is advantageous in these affinity studies, as it precludes the complexity introduced by the avidity of multivalent antigens. J558L cells expressing an endogenous Igλ1 light chain and Igβ, and a transfected Igα containing a YFP in its C terminus (Igα-YFP), were further transfected with cDNAs encoding mutant versions of the NIP-specific μ-B1-8 heavy chain that contained a CFP at their C termini (μ-B1-8-CFP). Point mutations were introduced into the μ-B1-8 heavy chain V regions to generate BCRs with either high affinity (W33L) or low affinity (A24G, S31T, H35Q, and R98T) mIgMs, as previously reported (Allen et al., 1988; Shih et al., 2002a,b). The B1-8-High and B1-8-Low antibodies showed a 50-fold difference in affinity for the hapten NIP, as measured by surface plasmon resonance ($K_A = 5.2 \times 10^8$ vs. 9.9×10^6; Fig. S1, A and B). We also observed that unlike the B1-8 antibody, the B1-8-High antibody showed no specific binding to the hapten 4-nitrophenylacetic acid (pNP), indicating that the W33L mutation abolished the specific recognition of this hapten, allowing pNP to be used as a nonspecific antigen control in subsequent experiments (Fig. S1 C). J558L cell lines stably expressing equivalent levels of μ-B1-8-High and μ-B1-8-Low BCRs (termed μ-High and μ-Low J558L cells, respectively) were acquired by cell sorting after hygromycin selection (Fig. S2, A–D). Using fluorescence microscopy we confirmed that μ-High and μ-Low J558L cells expressed Igα, Igβ, and mIgM on their surfaces and recognized NIP1-His12 (Fig. S2, A–C). The cells were labeled with Alexa Fluor 568–conjugated Fab IgM–specific antibodies (Alexa Fluor 568–Fab anti-IgM) under conditions that allowed tracking of individual BCRs placed on antigen-containing lipid bilayers by TIRFM. The fluorescence intensity (FI) profiles and bleaching characteristics of the individual spots indicated that they corresponded to single BCR molecules, as reported previously (Tolar et al., 2009a).

When placed on NIP-containing bilayers, we observed that the μ-High and μ-Low J558L cells spread and contracted slowly and inefficiently compared with the robust two-phase spreading and contraction responses described by Fleire et al. (2006) for HEL-specific primary B cells and confirmed in our recent studies for NIP-specific B1-8 primary B cells (Tolar et al., 2009a). The inability to spread is perhaps not surprising, as the parent J558L cells lack the expression of many coreceptors and adaptors that may be necessary to trigger the spreading and contraction responses, including CD19, which was recently described to be required for B cell spreading on antigen-containing lipid bilayers (Wienands et al., 1996; Adachi et al., 2001; Depoil et al., 2008). The slow, inefficient spreading and contraction of the μ-High and μ-Low J558L cells on the bilayer allowed the analysis of the behavior of BCRs as they first engaged antigen in the absence of this highly dynamic response (Video 1). Tracking single BCR molecules on μ-High and μ-Low J558L cells placed on bilayers that contained no antigen showed that their short-range mean square displacements (MSDs) were linearly dependent on time, indicating that their short-range movement was consistent with free diffusion (Fig. 1, A and C). The short-range diffusion coefficients of >2,000 individual BCR molecules were calculated, and their distribution was analyzed and displayed as a cumulative probability distribution (CPD) plot (Fig. 1 D). In the absence of antigen, only a small fraction (~20%) of BCRs in either the μ-High or μ-Low J558L cells were immobile with a cutoff diffusion coefficient of 0.01 $\mu m^2/s$ (Fig. 1, A and D), and the majority of BCRs of the μ-High and μ-Low J558L cells showed similar mean diffusion coefficients (Fig. 1, A and E; and Video 1, left). In contrast, the behavior of the BCRs was significantly different in the μ-High and μ-Low J558L cells placed on NIP1-His12–containing bilayers (Fig. 1, B–E; and Video 1, right). Fitting of the MSD plots into a confined diffusion mathematical model indicated that the BCRs in the μ-High cells were confined to an area smaller than that of the μ-Low cells (0.11 vs. 0.27 μm^2; Fig. 1, B and C). A larger fraction of BCRs in the μ-High cells was in immobilized oligomers (~54%) as compared with μ-Low cells (~39%; Fig. 1, B and D). The mean diffusion coefficient of the BCRs was significantly smaller for μ-High compared with μ-Low J558L cells (0.039 vs. 0.069 $\mu m^2/s$; Fig. 1, B and E).

Similar results were obtained in analyses of primary splenic B cells from $Igh^{B1\text{-}8/B1\text{-}8}/Ig\kappa^{-/-}$ transgenic mice that express the μ-B1-8 BCR (B1-8 primary B cells) that has a low affinity for the hapten pNP and a 250-fold greater affinity for NIP ($K_A = 1.7 \times 10^5$ vs. 4.2×10^7), as reported and confirmed in this study (Fig. S1, E and F). The BCRs of B1-8 primary B cells placed on lipid bilayers containing the high affinity hapten NIP1-His12 compared with the low affinity hapten pNP1-His12 showed a significantly smaller area of confinement (0.09 vs. 0.18 μm^2; Fig. 1 F), a larger fraction of immobilized oligomers in CPD plots (61 vs. 37%; Fig. 1 G), and a lower mean diffusion coefficient (0.03 vs. 0.07 $\mu m^2/s$; Fig. 1 H).

Collectively, these data indicate that the increased affinity of the BCRs facilitated their confinement and formation of immobile oligomers in response to membrane-associated antigens. Thus, the discrimination of antigen affinity appears to be a BCR-intrinsic event in the earliest stages of BCR clustering.

The accumulation of BCRs and antigen in the B cell's contact area with the membrane

We next determined the effect of BCR affinity on several additional early events in B cell activation, including the ability of cells to concentrate BCRs and antigen at the interface of the B cells and the bilayers, and the growth of individual BCR and antigen clusters in terms of FI and size. To do so, the μ-High or μ-Low J558L cells were labeled with Alexa Fluor 568–Fab anti-IgM and placed on lipid bilayers that contained either

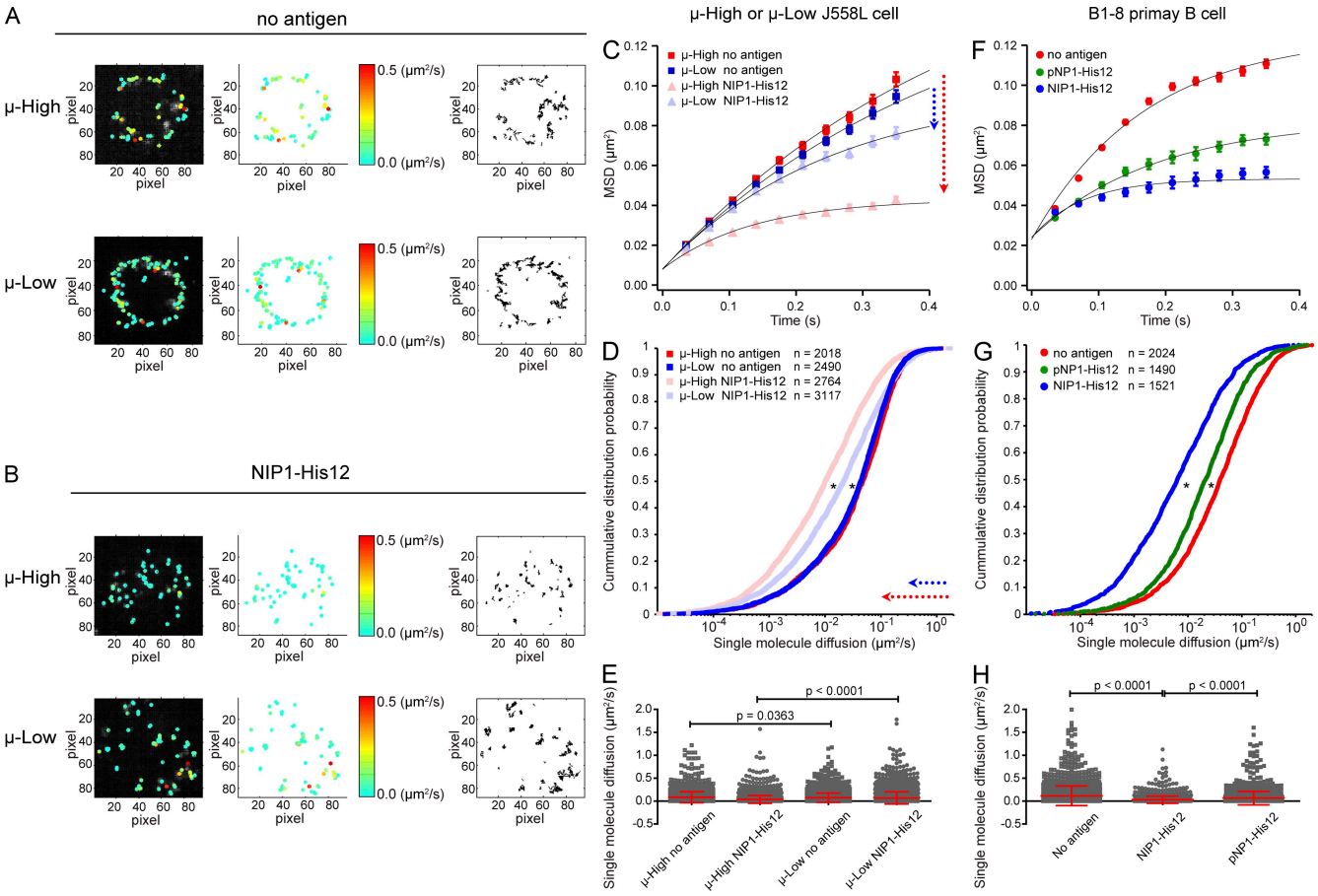

Figure 1. High affinity BCRs show an enhanced ability to form immobile oligomers. (A and B) The μ-High and μ-Low J558L cells labeled with Alexa Fluor 568–Fab anti-IgM were placed on planar lipid bilayers lacking antigen (A) or containing NIP1-His12 (B), and single BCR molecule TIRF images were acquired. (left and middle) Individual BCR molecules in TIRF images from one typical μ-High or μ-Low J558L cell (Video 1) indicating the instant diffusion coefficient (D_0) by pseudocolored spots. The display range of the pseudocolor is based on the D_0 value of 0–0.5 μm²/s, a range that included most of the D_0 values of the tracked BCRs (see E). (right) The accumulated trajectory footprints of individual BCR molecules in the entire time course. (C–H) The D_0 values for all BCR molecules from μ-High and μ-Low J558L cells (C–E) or B1-8 primary B cells (F–H) labeled with Alexa Fluor 568–Fab anti-IgM placed on planar lipid bilayers containing no antigen, NIP1-His12, or pNP1-His12. All of the D_0 values were displayed as MSD plots (C and F), CPD plots (D and G), or mean ± SD scattered plots (E and H). In C and D, the arrows indicate the change in the MSD (C) or single-molecule diffusion (D) for μ-High BCRs (red) and μ-Low BCRs (blue). Data represent single BCR molecules of the indicated numbers (D and G) for each condition from three independent experiments. The MSD plots (C and F) were further mathematically fitted into a confined diffusion model by an exponential function to acquire the size of the confinement microdomains, as detailed in Materials and methods. Significant differences by the Kolmogorov-Smirnov test are indicated (*, $P < 0.0001$) in D and G. One-tailed *t* tests were performed for statistical comparisons in E and H.

NIP1-His12, pNP1-His12, or NIP1-His12-Hylight647 at concentrations of 10 or 50 nM, as previously described (Tolar et al., 2009a). The cells were examined every 2 s beginning with the initial contact of the cells with the membranes by collecting images of Igα-YFP with either Alexa Fluor 568–Fab-anti-IgM or NIP1-His12-Highlight647 in two-color TIRFM (Fig. S2 E). Compared with the μ-Low J558L cells, the μ-High J558L cells accumulated significantly more BCRs and antigens in the contact area in a 120-s time course, as indicated by the increased mean FI of Igα-YFP (Fig. 2 A and Video 2), Alexa Fluor 568–Fab anti-IgM (Fig. 2 B and Video 3), and NIP1-His12-Hylight647 (Fig. 2 C and Video 4). The accumulation of both the BCRs and antigen was antigen-dependent in that no accumulation occurred when the μ-High J558L cells were placed on bilayers that did not contain antigen (Fig. 2, D and E) or contained an antigen for which the μ-High J558L cells were not specific (i.e., pNP1-His12; Fig. 2, D and E). These results are consistent with the earlier results of Fleire et al. (2006), who showed that the accumulation of the BCRs and antigen in the contact area between the B cell and an antigen-containing bilayer was BCR affinity dependent.

The growth of BCR microclusters

We next characterized the growth of individual BCR microclusters with time after they initially formed after contact with antigen-containing bilayers first using the images of μ-High J558L cells. The growth of the BCR microclusters was quantified by both size (the diameter of the fluorescence signal)

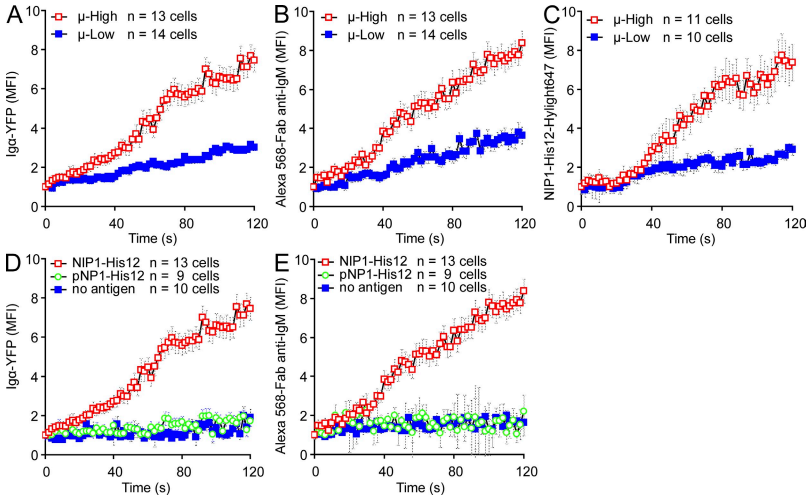

Figure 2. Accumulation of BCRs and antigen into the contact area between B cells and antigen-containing planar lipid bilayers is affinity dependent. (A–C) The mean FI (MFI) within the contact area of Igα-YFP (A), Alexa Fluor 568–Fab anti-IgM (B), or NIP1-His12-Hylight647 (C) is given over a 120-s time course (Videos 2–4) for μ-High and μ-Low J558L cells placed on planar lipid bilayers containing NIP1-His12 (A and B) or NIP1-His12-Hylight647 (C). (D and E) MFI of either Igα-YFP (D) or Alexa Fluor 568–Fab anti-IgM (E) is given over a 120-s time course for μ-High J558L cells placed on planar lipid bilayers containing no antigen, NIP1-His12, or pNP1-His12. The data represent means ± SEM of 9–14 B cells from three independent experiments.

and the integrated FI. To obtain accurate information on the size and the FI of each microcluster at each time point, all Alexa Fluor 568 and YFP microclusters were analyzed by fitting them individually to a two-dimensional (2D) Gaussian function (Holtzer et al., 2007). For each microcluster, the 2D Gaussian fit yields the parameters of position (x_c, y_c) for x and y coordinates, integrated FI for the quantification of FI, and full width at half-maximum peak height (FWHM; σ_x, σ_y) of the intensity distribution in the x and y direction for the quantification of size (Fig. S4 A; Holtzer et al., 2007). Only the first 120 s of each track of the microclusters was analyzed to minimize tracking and Gaussian fitting errors, both of which arise from microclusters merging and overlapping at later times. Typical examples of the growth of individual clusters in the imaging time course are depicted (Fig. 3, A–C; Fig. 4 A; and Video 5). The μ-High J558L cells formed microscopic BCR clusters at the initial contact points between the cells and the NIP1-His12–containing membrane (Fig. 3 A). These clusters obviously grew in FI with time (Fig. 3 B and Fig. 4 A), and these were stationary and did not move over a 2-pixel (300-nm) range over the entire time course (Fig. 3 C and Video 5). The growth of the BCR clusters with time was antigen dependent, as stable clusters did not form or grow on bilayers that did not contain antigen or contained the antigen pNP1-His12, which the μ-High J558L cells do not recognize (Fig. 3, D–F; Fig. 4 B; and Video 5). The microscopic BCR clusters that appear in B cells placed on bilayers that do not contain antigen were shown previously to contain highly mobile BCRs diffusing in an area of confinement, likely imposed by membrane topology (Tolar et al., 2009a). In contrast, microscopic BCR clusters in B cells placed on antigen-containing bilayers contain immobile BCR oligomers, as shown in Fig. 1 and Video 1.

A comparison of hundreds of BCR microclusters analyzing the FI of Igα-YFP or Alexa Fluor 568–Fab anti-IgM showed the increase in FI of individual clusters to be rapid, with the FI increasing 30-fold over 120 s (Fig. 3, G and H). The growth of the microclusters' FI was antigen dependent, although we did observe a slight, two- to three-fold, transient increase in FI within the first 40 s in the initial contact points of the μ-High J558L cells with the bilayers that did not contain antigen (Fig. 3, E, G, and H). This increase in FI may simply reflect the increase in FI with enhanced illumination in the TIRF field as the B cell approaches the coverslip. Alternatively, this increase in FI may represent an antigen-independent accumulation of BCRs in the first contact points between the cells and the lipid bilayer. In experiments described in the next section simultaneously imaging the FI of Igα-YFP and NIP1-His12-Hylight647 of the μ-High J558L cells placed on lipid bilayers containing NIP1-His12-Hylight647, we observed colocalization of YFP and Hylight647 and simultaneous growth of the FIs of both YFP and Hylight647 microclusters, indicating that the growth of microclusters is caused by an increase in antigen-engaged BCRs (see Fig. 5, A–C; Fig. S2 E; Fig. S3 A; and Video 6).

We next focused on the size (diameter) of the BCR microclusters (Fig. 4 and Fig. S4). Examples of the increase in microcluster size imaging either Igα-YFP or Alexa Fluor 568–Fab anti-IgM for the μ-High J558L cells on antigen-containing bilayers (Fig. 4 A and Video 5) or on bilayers that did not contain antigen are depicted (Fig. 4 B and Video 5). Averaging the data from a large number of clusters, we observed that the microclusters grew in size very little over the first 30 s (Fig. 4, C and D). When first detected, at the beginning of the tracking, the microclusters were of a mean size of 479 ± 14 nm for YFP clusters and 446 ± 12 nm for Alexa Fluor 568 clusters. During the first 30 s, the BCR microclusters were of similar size in cells placed on bilayers that did or did not contain antigen (Fig. 4, C and D). Although the microclusters did not dramatically increase in size during the first 30 s, they increased in FI nearly 10-fold (Fig. 3, G and H). Between 30 and 120 s, the microclusters increased more than twofold in size in an antigen-dependent manner (Fig. 4, A–D). The FI continued to increase to nearly 30-fold of the initial value during this time (Fig. 3, G and H).

We also examined the correlation of the FI and the size of the BCR microclusters to determine if there is a relationship between the FI and the size of a microcluster (Fig. S4 B). A linear regression of the paired values of FI and the size of

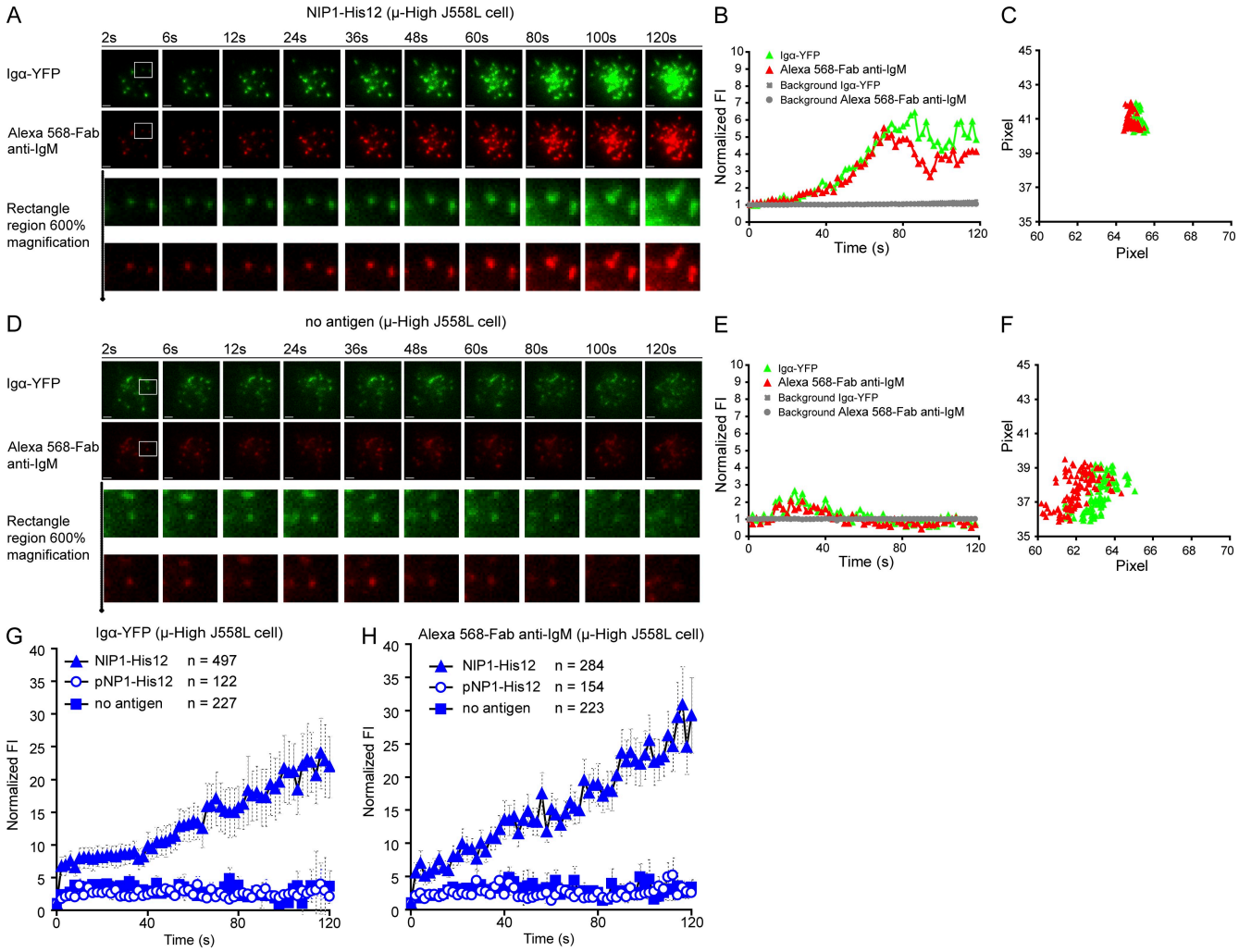

Figure 3. BCR microclusters grow in FI with time when encountering antigen-containing lipid bilayers. (A–F) Shown are two-color time-lapse TIRF images of μ-High J558L cells labeled with Alexa Fluor 568–Fab anti-IgM placed on planar lipid bilayers containing antigen NIP1-His12 (A–C) or lacking antigen (D–F) over a time course of 120 s (Video 5). The BCR microclusters were examined by simultaneously imaging Igα-YFP (green) and Alexa Fluor 568–Fab anti-IgM (red), as described in Materials and methods. Bars, 1.5 μm. Typical microclusters in the images indicated by the white boxes are shown at 600% magnification for better resolution. The FIs of these microclusters were fitted by a 2D Gaussian function for precise 2D (x, y) coordinates and integral FI profiles, as detailed in Materials and methods. The normalized FI (B and E) and 2D trajectories by means of x versus y footprints (C and F) accumulated over the 120-s time course of these two typical microclusters are given. The gray horizontal lines in B and E show the background FI values for these two typical microclusters over time. The background FI value is the Z_0 value acquired in the 2D Gaussian function upon mathematical fitting, as shown in Fig. S4 A. The normalized FIs of all BCR microclusters analyzed by Igα-YFP (G) or Alexa Fluor 568–Fab anti-IgM (H) in μ-High J558L cells placed on lipid bilayers containing no antigen, NIP1-His12, or pNP1-His12 represent means ± SEM from 9–13 μ-High J558L cells in three independent experiments. For Igα-YFP clusters, data from six experiments were pooled.

all the BCR microclusters over the entire time course showed a strong positive correlation between the FI and the size of BCR microclusters analyzing either Igα-YFP or Alexa Fluor 568–anti-IgM (Fig. 4, E and F). This indicates that BCR microclusters grow proportionately in size and in the number of BCRs in the clusters. This positive correlation did not hold for a linear regression analysis of BCR microclusters in μ-High J558L cells placed on bilayers that did not contain antigen (Fig. 4, E and F).

Collectively, these results show that BCR microclusters grow with time in both FI and size. The growth in FI appears linear, whereas the growth in size appears to have at least two phases, suggesting that the size of the microcluster tolerates the initial accumulation of BCR and antigens, and only increases after some maximal number of BCRs accumulates in the cluster.

The growth of BCR microclusters is antigen concentration dependent and selective

The increase in FI and the growth in size of antigen microclusters were analyzed from the images of μ-High cells placed on bilayers that contained 10 or 50 nM NIP1-His12-Hylight647,

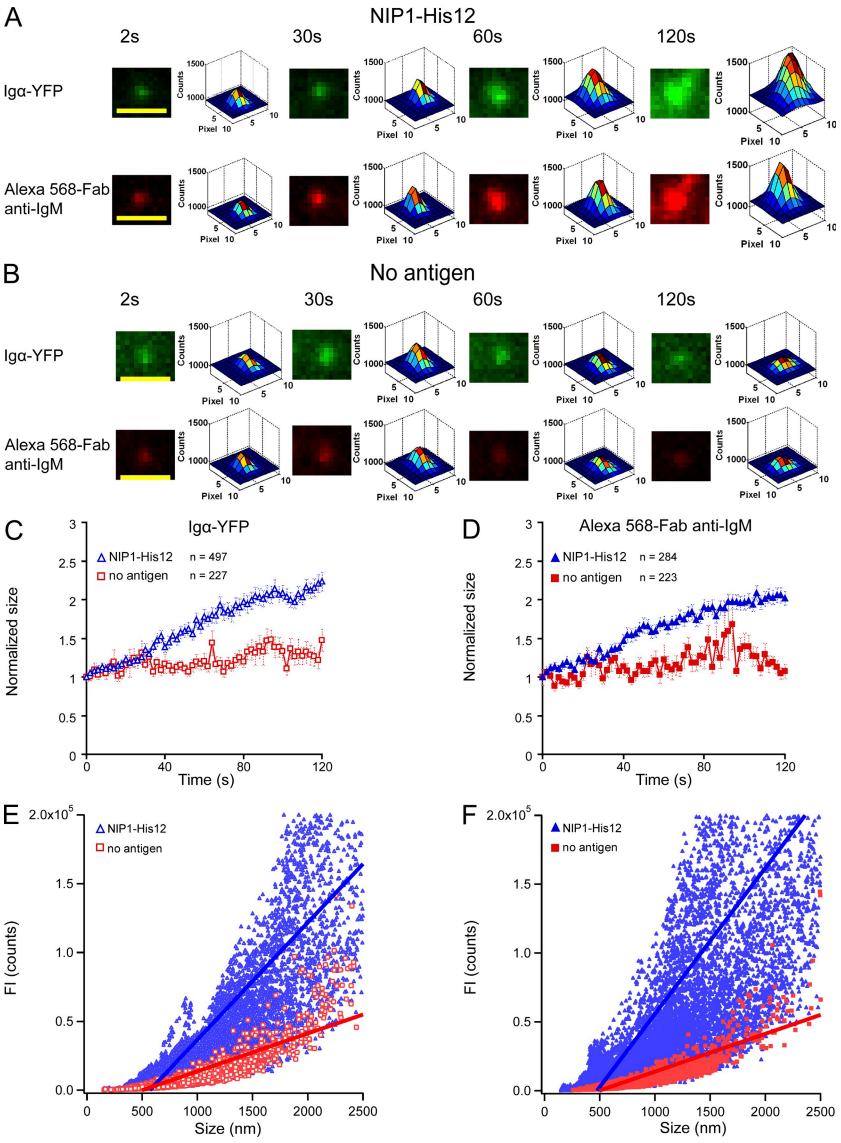

Figure 4. BCR microclusters grow in both size and FI with time when encountering antigen-containing lipid bilayers. (A and B) Pseudocolor 2.5D Gaussian images of one typical Igα-YFP or Alexa Fluor 568–Fab anti-IgM microcluster are shown at the indicated times (Video 5) for μ-High J558L cells placed on planar lipid bilayers containing NIP1-His12 (A) or lacking antigen (B). The FWHM of each BCR microcluster upon 2D Gaussian fitting was used as a measure of the size of the microclusters, as detailed in Materials and methods and Fig. S4 A. Bars, 1.5 μm. (C and D) Means ± SEM of the normalized size of BCR microclusters analyzed by Igα-YFP (C) or Alexa Fluor 568–Fab anti-IgM (D) are given at the indicated time points for μ-High J558L cells placed on planar lipid bilayers containing NIP1-His12 or lacking antigen. Data represent the indicated numbers of BCR microclusters examined in three independent experiments. (E and F) Linear regression analyses of the FI and the size of BCRs. The slopes of the linear fitting for μ-High J558L cells placed on planar lipid bilayers containing NIP1-His12 antigen were 85 (Igα-YFP; E) and 106 (Alexa Fluor 568–Fab anti-IgM; F). The slopes for μ-High J558L cells placed on planar lipid bilayers containing no antigen were each 27 (E and F).

or 10 or 50 nM NIP1-His12, and compared with the growth of BCR clusters imaged as Igα-YFP or Alexa Fluor 568–Fab anti-IgM. As depicted, for a single cell, YFP and NIP1-His12-Hylight647 colocalized in clusters (Fig. 5 A) and grew in FI similarly (Fig. 5 B). The increase in FI for a large number of BCR and antigen clusters is also given (Fig. 5 C) and shows the simultaneous increase in FI of BCR and antigen clusters. An analysis and comparison of cluster FI and size for Igα-YFP (Fig. 5, G and K), Alexa Fluor 568–Fab anti-IgM (Fig. 5, H and L), and NIP1-His12-Hylight647 (Fig. 5, I and M) show that the increase in cluster FI and the growth in cluster size are antigen concentration dependent.

We also determined that the accumulation of BCRs in microclusters and the resulting growth of the microclusters are selective in that MHC class I molecules showed no stable accumulation in the microclusters. To do so, the μ-High J558L cells labeled with Cy3-conjugated Fab MHC class I–specific antibodies (Cy3–Fab anti–MHC I) were placed on lipid bilayers that contained no antigen or 10 or 50 nM NIP1-His12. Igα-YFP and Cy3–Fab anti–MHC I microclusters were analyzed simultaneously in time-lapse two-color TIRF imaging (Fig. S2 E). Examples of the growth of individual clusters are depicted (Fig. 5, D and E; and Fig. S3 B). The size and the FI of the BCR microclusters increased with time (Fig. 5 E and Fig. S3 B); in contrast, MHC molecules did not stably accumulate through the 120 s of the analysis (Fig. 5, D and E; and Video 7), even at higher NIP1-His12 concentrations (Fig. 5, J and N). A comparison of the average of hundreds of BCR microclusters showed a small increase in the FI of Cy3–Fab anti–MHC I during the first 10–20 s of the analysis (Fig. 5 F). We speculate that this increase in FI may reflect a phenomenon similar to the nonspecific accumulation of individual BCRs in BCR microclusters during the first several seconds of contact between the cells and lipid bilayers that did not contain antigen. However, the small increase in FI for MHC class I molecules did not appear for B cells on bilayers that did not contain antigen, suggesting that the BCR's engagement was driving the accumulation.

The growth of BCR microclusters is affinity dependent

The growth of BCR microclusters was compared between images of the μ-High and μ-Low J558L cells placed on lipid bilayers containing NIP1-His12-Hylight647. As measured by either the FI or the size of the Igα-YFP, Alexa Fluor 568–Fab anti-IgM, or NIP1-His12-Hylight647 microclusters,

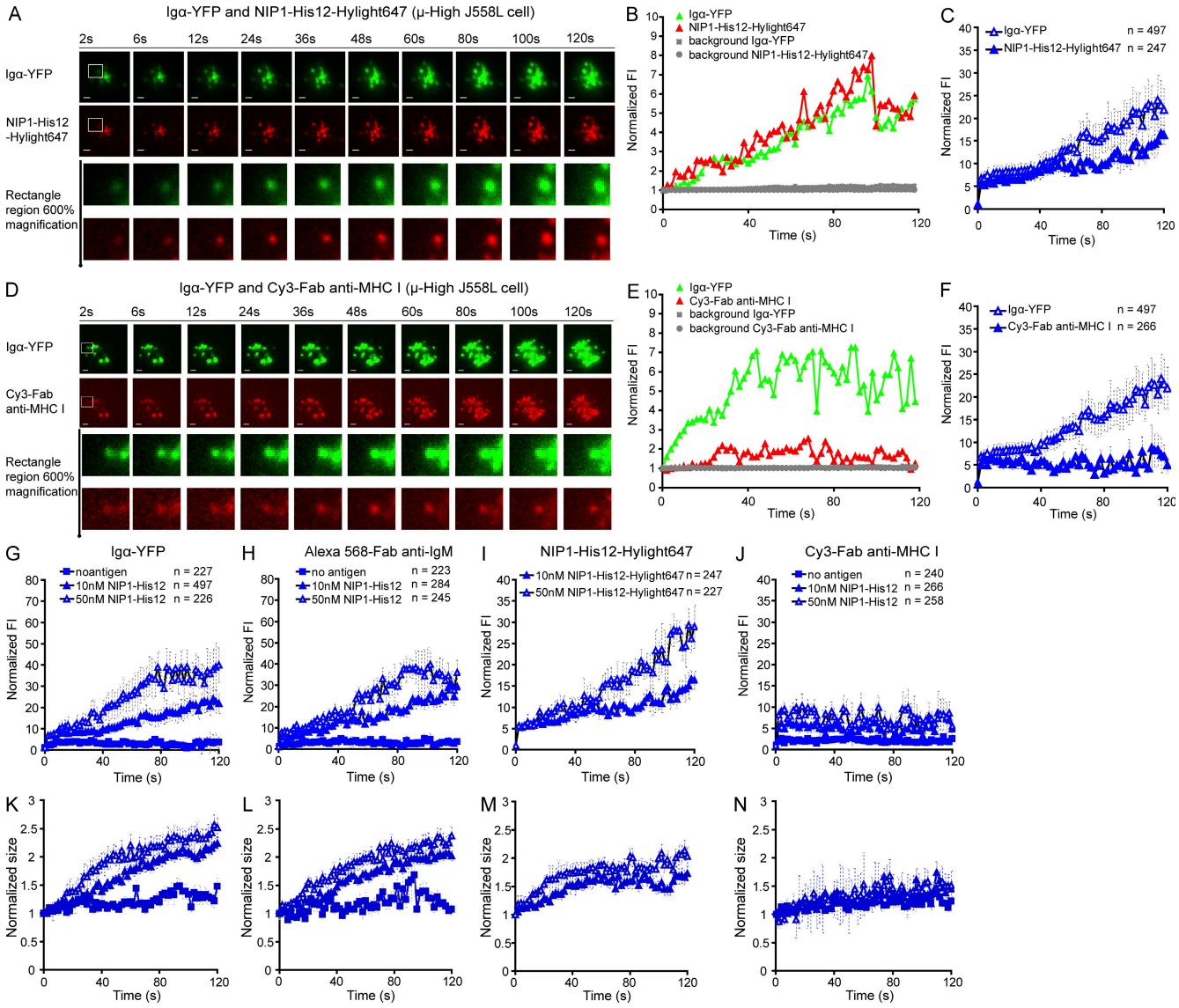

Figure 5. The growth of BCR microclusters is selective and antigen concentration dependent. (A–F) Two-color time-lapse TIRF images of Igα-YFP (green) and NIP1-His12-Hylight647 (red) are given at the indicated time points (Video 6) for μ-High J558L cells placed on planar lipid bilayers containing NIP1-His12-Hylight647 (A). Similarly, two-color time-lapse TIRF images of Igα-YFP (green) and Cy3-Fab anti-MHC I (red) are given at the indicated time points (Video 7) for μ-High J558L cells placed on planar lipid bilayers containing NIP1-His12 (D). Bars, 1.5 μm. (A and D, bottom) Typical microclusters magnified 600% and analyzed by 2D Gaussian fitting. Shown are the normalized FI for Igα-YFP and NIP1-His12-Hylight647 (B) and Igα-YFP and Cy3-Fab anti-MHC I (E). The gray horizontal lines in B and E show the background FI values for these two typical microclusters over time. The background FI value is the Z_0 value acquired in the 2D Gaussian function upon mathematical fitting, as shown in Fig. S4 A. Normalized FI of all Igα-YFP and NIP1-His12-Hylight647 clusters (C) or Igα-YFP and Cy3-Fab anti-MHC I clusters (F) are given with time. (G–N) The normalized FI (G–J) and size (K–N) of microclusters examined by Igα-YFP (G and K), Alexa Fluor 568–Fab anti-IgM (H and L), NIP1-His12-Hylight647 (I and M), or Cy3-Fab anti-MHC I (J and N) are given for μ-High J558L cells placed on lipid bilayers lacking antigen or containing NIP1-His12 antigen at a concentration of 10 nM (25 molecules/μm^2) or 50 nM (100 molecules/μm^2). The data represent means ± SEM of the indicated numbers of clusters in three independent experiments.

BCR microclusters on the μ-High J558L cells grew in FI and size more rapidly compared with the microclusters on the μ-Low J558L cells placed on lipid bilayers containing 25 molecules/μm^2 of NIP-1-His12 (Fig. 6, A–C, J, and K; Fig. S5, A–D; and Video 8). The dependence of the growth of BCR microclusters on BCR affinity was also observed for the μ-High and μ-Low J558L cells placed on lipid bilayers containing 100 molecules/μm^2 of NIP-1-His12 (Fig. 6, D–F; and Fig. S5, E–G).

Similar results were obtained comparing the rate of accumulation of BCRs of naive splenic B1-8 primary B cells. The B1-8 primary B cells were observed to first spread and then contract on antigen-containing bilayers, and consequently, the BCR microclusters were only analyzed for the

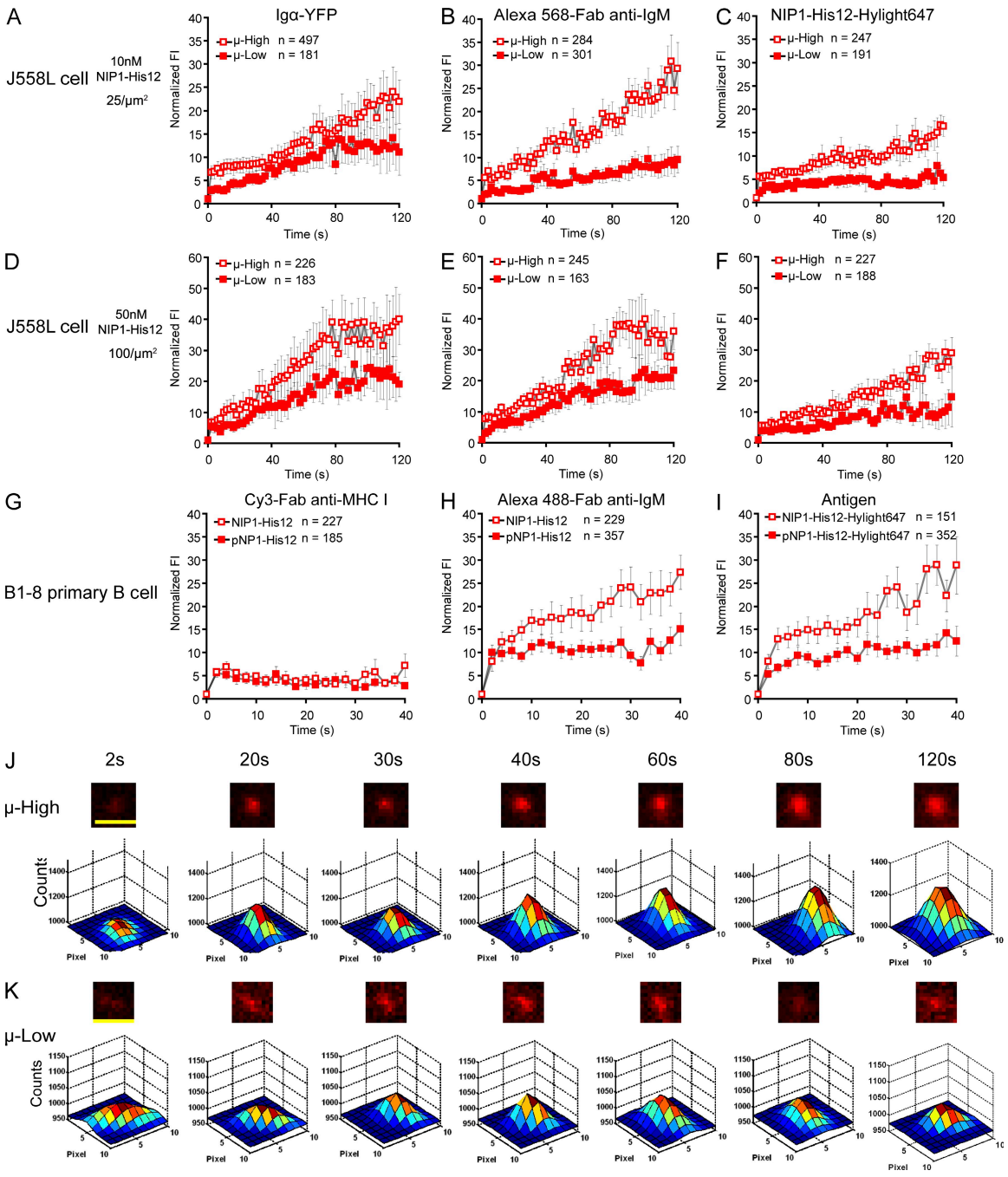

Figure 6. The growth in FI of BCR microclusters is antigen affinity dependent. (A–F) The normalized FI of BCR microclusters examined by Igα-YFP (A and D) and Alexa Fluor 568–Fab anti-IgM (B and E) or of antigen microclusters examined by NIP1-His12-Hylight647 (C and F) are given with time (Video 8) for μ-High or μ-Low J558L cells placed on planar lipid bilayers containing NIP1-His12 (A, B, D, and E) or NIP1-His12-Hylight647 (C and F) at a concentration of 10 nM (25 molecules/μm²) or 50 nM (100 molecules/μm²), as indicated. (G–I) The normalized FIs of Cy3–Fab anti–MHC I (G), IgM–Alexa Fluor 488 (H), and NIP1-His12-Hyligh647 (or pNP1-His12-Hyligh647; I) microclusters are given for B1-8 primary B cells placed on planar lipid bilayers containing the high affinity antigen NIP1-His12 or the low affinity antigen pNP1-His12. In A–I, the data represent means ± SEM of indicated numbers of microclusters in three independent experiments. (J and K) Also given are pseudocolor 2.5D Gaussian images of typical antigen microclusters examined by NIP1-His12-Hylight647 at the indicated times for μ-High (J) or μ-Low (K) J558L cells placed on antigen-containing lipid bilayers. The FWHM of each microcluster upon 2D Gaussian fitting was used as a measure of the size of the microclusters, as detailed in Materials and methods and Fig. S4 A. Bars, 1.5 μm.

first 20 frames (40 s) before the individual BCR microclusters moved and merged into the center IS after the contraction of the B1-8 primary B cells (Fig. 6, G–I; Fig. S6; and Video 9). The growth of the BCR microclusters was much faster and reached higher maximal levels for B1-8 primary B cells placed on lipid bilayers containing the high affinity

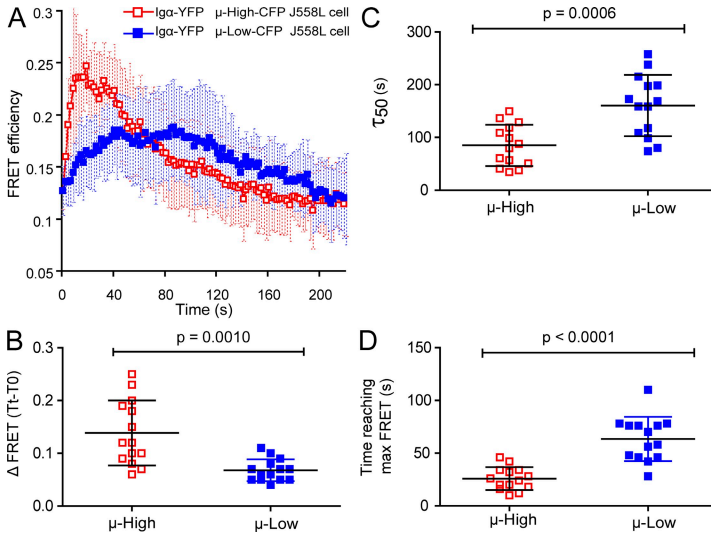

Figure 7. BCR oligomerization–induced conformational changes in the BCR's cytoplasmic domain are affinity dependent. FRET efficiencies between FRET donor Igα-YFP and FRET acceptor μ-CFP are given at the indicated time points for μ-High or μ-Low J558L cells placed on lipid bilayers containing NIP1-His12. (A) Means ± SD of FRET efficiencies are given over a time course of 240 s. (B and D) Statistical comparisons for the maximal changes in FRET (ΔFRET) from 0 and 200 s (B) and the time needed to reach maximal FRET efficiency (D) are given for μ-High and μ-Low J558L cells. (C) The half-life of FRET loss (τ_{50}) of FRET efficiencies from maximal FRET levels in both μ-High and μ-Low J558L cells were acquired by fitting the FRET loss plot of individual cells into a monoexponential decay function, as detailed in Materials and methods. The bars represent means ± SD from 14 μ-High and μ-Low J558L cells in three independent experiments. Two-tailed *t* tests were performed for the statistical comparisons in B–D.

antigen NIP1-His12 compared with B cells placed on bilayers containing the low affinity antigen pNP1-His12 (Fig. 6, H and I). The growth of the BCR microclusters was antigen dependent, as no accumulation was observed for B1-8 primary B cells placed on bilayers that did not contain antigen, and selective, as no accumulation of MHC class I molecules was observed (Fig. 6 G).

Collectively, these results show that the growth of BCR microcluster is affinity dependent. The growth of the BCR microclusters occurs even though the J588L cells fail to undergo a two-phase spreading and contraction response, suggesting the BCRs intrinsically sense the affinity of the antigen.

BCR oligomerization–induced conformational changes in the BCR's cytoplasmic domain are affinity dependent

Our previous studies showed by FRET analyses that BCRs, when clustered after antigen binding, undergo a conformational change in their cytoplasmic domains from a closed to an open form that occurs simultaneously with the phosphorylation of the BCR's immunoreceptor tyrosine-based activation motifs (Tolar et al., 2005; Sohn et al., 2008). To determine if this change was affinity dependent, we analyzed FRET in J558L cells expressing the FRET donor μ-B1-8-High-CFP or μ-B1-8-Low-CFP and the FRET acceptor Igα-YFP with time after the cells were placed on an NIP1-His12–containing fluid lipid bilayer (Fig. 7 A). FRET was detected in both the μ-High and μ-Low J558L cells in the absence of antigen, reflecting the close molecular proximity of Igα and the μ heavy chain in individual BCRs, as previously described (Tolar et al., 2005; Sohn et al., 2008). In both cell lines, antigen induced a rise in FRET as the BCRs formed microclusters and a subsequent decrease in FRET as the cytoplasmic domains opened. However, both the kinetics and magnitude of the FRET changes were markedly different in the μ-High versus μ-Low J558L cells (Fig. 7). Compared with the μ-Low J558L cells, the μ-High J558L cells showed a more rapid acquisition of FRET that reached higher levels and decreased more rapidly (Fig. 7, A–D). Focusing on the loss of FRET, a change that we previously showed occurs simultaneously with BCR phosphorylation, we applied a monoexponential decay fitting to acquire the mathematical half-life of FRET loss (τ_{50}) for individual μ-High and μ-Low J558L cells. For μ-High J558L cells, τ_{50} was 85.04 ± 10.48 s, and for μ-Low J558L cells, τ_{50} was 160.45 ± 15.53 s (mean ± SEM; Fig. 7 C). Thus, there is nearly a twofold difference in the rate at which the high affinity BCRs clusters come into a signaling-active conformation.

The affinity-dependent growth of BCR microclusters correlates with the strength of signaling

To determine if the faster accumulation of BCRs into microclusters during the first 120 s resulted in enhanced recruitment of Syk into BCR microclusters at a later time point, μ-High and μ-Low J558L cells were placed on antigen-containing bilayers for 10 min, fixed, permeabilized, and stained with antibodies specific for phosphorylated Syk (pSyk). TIRF imaging of the entire contact area showed that although the contact areas of the μ-High and μ-Low J558L cells were similar in size at 10 min (Fig. 8, A and B, middle), in μ-High J558L cells significantly more BCRs were clustered in the contact area and significantly larger numbers of pSyk molecules were recruited to the contact area as compared with μ-Low J558L cells (Fig. 8, A and B). Similar results were obtained when comparing B1-8 primary B cells placed on lipid bilayers containing the high affinity antigen NIP1-His12 versus the low affinity antigen pNP1-His12 (Fig. 8, C and D). These data are consistent with the results given in Fig. 7 showing that the BCRs on μ-High J558L cells both clustered more rapidly into a closed conformation and opened more rapidly into a signaling-active conformation that could be phosphorylated and recruit Syk. In addition, calcium fluxes in the B1-8 primary B cells placed on lipid bilayers containing the high affinity antigen NIP1-His12 were more rapid and reached higher maximums compared with those placed on lipid bilayers containing the low affinity antigen pNP1-His12 (Fig. S7 and Video 10).

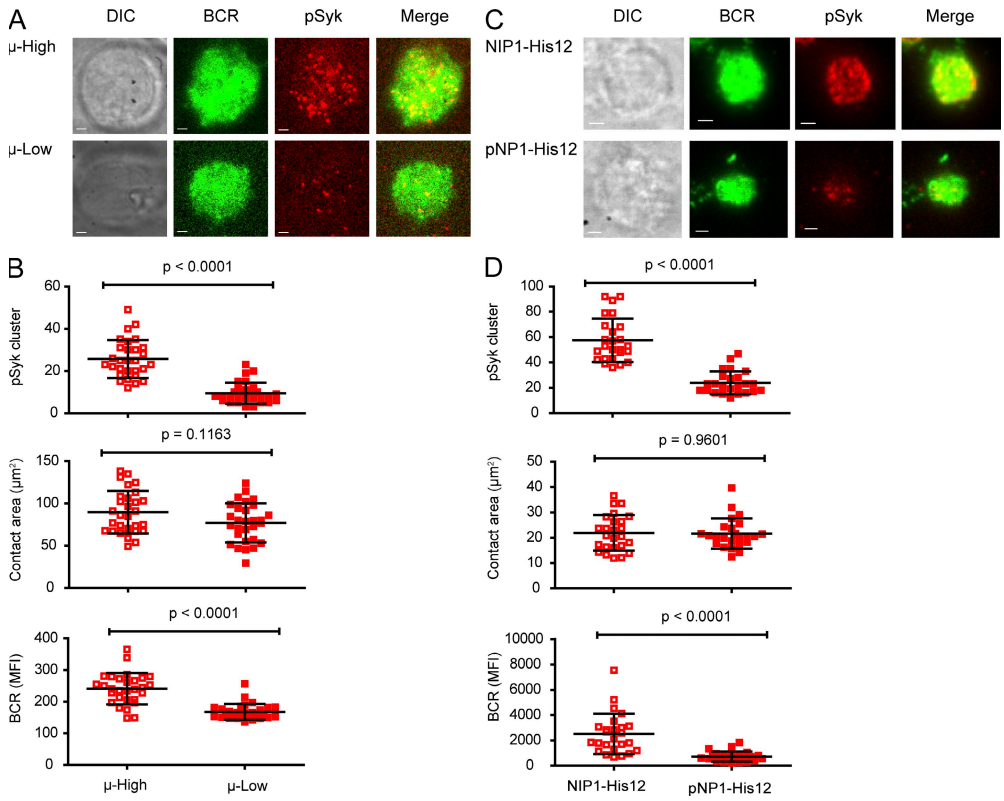

Figure 8. The affinity-dependent growth of BCR microclusters correlates with the strength of signaling. (A and B) μ-High and μ-Low J558L cells were fixed 10 min after placing them on lipid bilayers containing NIP1-His12 antigen. (C and D) B1-8 primary B cells were fixed 10 min after placing on lipid bilayers containing high affinity antigen NIP1-His12 or low affinity antigen pNP1-His12. The fixed B cells were probed for the recruitment of pSyk into the contact area of the B cells with the lipid bilayer by intracellular staining for pSyk. Shown are two-color TIRF images for BCR and pSyk (A and C). Bars, 1.5 μm. (B and D) The number of pSyk clusters accumulated in the contact area (top), the size of the contact area (middle), and mean BCR FI of the contact area (bottom). Each dot represents one cell analyzed in three independent experiments, and bars represent means ± SD. Two-tailed *t* tests were performed for the statistical comparisons in B and D. DIC, differential interference contrast.

The cellular requirements for the growth of BCR microclusters

Our previous studies demonstrated that the formation of immobile BCR oligomers was BCR intrinsic and did not require a signaling-competent BCR (Tolar et al., 2009a). Less is known about the requirements for the affinity-dependent growth of BCR clusters described in the previous section. To determine the requirement for signaling and the cell's actin and microtubule networks for BCR microcluster growth, the μ-High J558L cells were treated with various inhibitors or DMSO as a control, labeled with Alexa Fluor 568–Fab anti-IgM, and placed on antigen-containing lipid bilayers. TIRF images of Alexa Fluor 568 were obtained. The μ-High J558L cells treated with DMSO as a control showed stable growth of BCR microclusters (Fig. 9, A–C). The BCRs in the μ-High J558L cells treated with PP2 to block Src family kinases or with piceatannol to block Syk initially clustered, and these clusters grew for the first 60 s at a similar rate to that of BCRs in DMSO-treated control cells (Fig. 9 A). However, the microclusters in PP2- or piceatannol-treated cells stopped growing after 60 s. This observation suggests that the early phases of BCR microcluster growth was BCR intrinsic and occurred in the absence of signaling through Lyn and Syk. However, continued growth of the clusters beyond 60 s was signaling dependent.

In contrast, the entire process of BCR microcluster growth was dependent on the actin cytoskeleton. In cells treated with latrunculin B to disrupt the actin cytoskeleton, BCR microclusters failed to grow in both the early and late phases (Fig. 9 B). As the growth of microclusters and the early recruitment of BCRs to these clusters were signaling independent, the early dependency of the cluster growth on the actin cytoskeleton likely reflects an indirect requirement for actin to retain the membrane topology necessary to confine BCRs and facilitate BCR immobilization rather than a need for direct interactions of the BCRs with the actin cytoskeleton. Interestingly, in B cells treated with jasplakinolide that stabilizes actin cytoskeleton filaments by blocking actin depolymerization, BCR microclusters also failed to grow (Fig. 9 B). Collectively, these observations suggest that the growth of BCR microclusters is highly dependent on the balanced dynamics of actin polymerization and that either disrupting or stabilizing actin filament polymerization blocks the growth of BCR microclusters. The microtubule polymerization inhibitor nocodazole had an effect

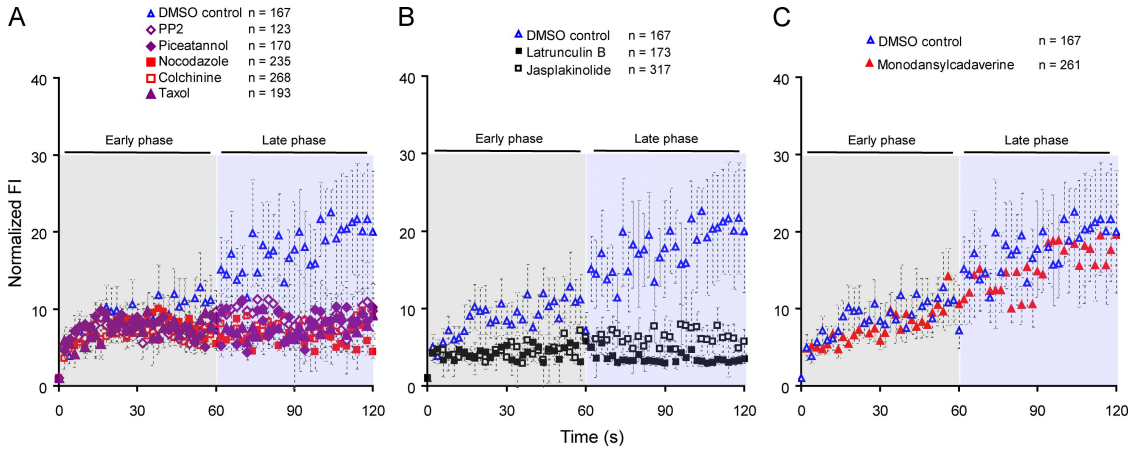

Figure 9. The cellular requirements for the growth of BCR microclusters. (A–C) The μ-High J558L cells were treated with DMSO or the inhibitors shown (as detailed in Materials and methods), labeled with Alexa Fluor 568–Fab anti-IgM, and placed on lipid bilayers containing 10 nM NIP1-His12. TIRF images of Alexa Fluor 568 were obtained. The normalized FIs of Alexa Fluor 568–Fab anti-IgM BCR microclusters with time are shown, grouped according to the effect of the inhibitors on the growth of BCR microclusters during the early phase of the response (0–60 s; gray-shaded area) and the late phase (60–120 s; blue-shaded area). The data represent means ± SEM of the indicated numbers of BCR microclusters in three independent experiments.

similar to the Lyn and Syk inhibitors, blocking the late but not early phase of microcluster growth (Fig. 9 A). Because earlier studies suggested that nocodazole inhibited T cell ZAP70-dependent signaling independent of its effects on the microtubule cytoskeleton (Huby et al., 1998), we pretreated μ-High J558L cells with two other microtubule inhibitors: colchicine to disrupt microtubule polymerization and taxol to stabilize microtubule polymerization. The effects on BCR cluster growth were similar to those obtained using nocodazole (Fig. 9 A), suggesting that the microtubule cytoskeleton is required for the sustained growth of BCR microclusters. Lastly, we observed that pretreatment of μ-High J558L cells with monodensylcadaverine to block BCR internalization had no effect on the growth of the BCR microclusters (Fig. 9 C). Collectively, these results suggest that the BCR microclusters grow in at least two phases: initially BCR intrinsic and then in a signaling- and cytoskeleton-dependent fashion.

DISCUSSION

Affinity maturation, the increase in the affinity of antigen-specific antibodies during the course of immune responses, is a central feature of humoral immunity (Griffiths et al., 1984; Berek et al., 1985; Foote and Milstein, 1991; Milstein, 1991). Classical models of affinity maturation hold that it is an antigen-driven process that occurs to a large extent in GCs, where B cells rapidly divide and somatically hypermutate their antibody V genes and are subsequently clonally selected based on the affinity of their BCRs for antigen (Takahashi et al., 1998; Dal Porto et al., 2002; Shih et al., 2002a,b; Brink et al., 2008). The mechanism by which clonal selection occurs is not well understood but has been suggested to involve competition for antigen, T cell help, or survival niches. In this model, selection is presumably caused by clonal competition between high and low affinity B cells whose BCRs have the same intrinsic ability to activate B cells (Shih et al., 2002a). In addition to clonal competition, recent studies provided evidence for a B cell–intrinsic mechanism for antigen affinity discrimination involving a dynamic signaling and actin-dependent spreading and contraction response of B cells encountering antigen on membranes (Fleire et al., 2006). In this paper, we provide evidence that the affinity of an antigen is discriminated by BCR-intrinsic mechanisms involved in the earliest events in antigen-driven BCR clustering that lead to the initiation of signaling. Using high resolution, live-cell imaging techniques, we provided evidence that compared with low affinity BCRs, high affinity BCRs oligomerize more readily, grow more rapidly, and adopt a signaling-active open conformation in their cytoplasmic domains more quickly. These differences were correlated with subsequent downstream enhanced recruitment of Syk and calcium responses.

Using single-molecule tracking, we first show that high affinity BCRs form immobile oligomers in response to membrane antigen more efficiently than low affinity BCRs. Our current model of antigen-induced BCR oligomerization that we refer to as the conformation-induced oligomerization model (Tolar and Pierce, 2010) holds that in resting B cells the BCR is highly mobile in the plane of the membrane but not in a conformation receptive to oligomerization. Consequently, random bumping of BCRs has no repercussion. Binding of antigen, including monovalent antigen, on an opposing membrane of an APC imposes a force on the BCR that results in a change in the BCR's Cμ4 domain so that the antigen-bound BCR is receptive to oligomerization, and if it encounters another antigen-bound BCR, the BCRs oligomerize. The results described in this paper provide evidence that this process is BCR affinity dependent, indicating that the more time a BCR spends bound to antigen and in an oligomerization-receptive form the more likely the BCR is to oligomerize. Thus, by this mechanism BCRs are able to read the affinity of the antigen at the earliest step in the formation of signaling-active BCR clusters.

Our earlier studies used FRET as a molecular ruler to determine both the distance between the intracellular chains within individual BCRs and between the intracellular domains of different BCRs (Tolar et al., 2005; Sohn et al., 2008). We observed that upon initial formation of microclusters, the cytoplasmic domains of BCRs were brought into close molecular proximity and gained FRET. Within seconds the FRET was lost and Syk was recruited to the BCR, suggesting that the BCR's cytoplasmic domains opened into a signaling-active form (Tolar et al., 2005; Sohn et al., 2008). The results presented in this paper show that the rate and magnitude of FRET gain and loss were markedly different for the μ-High versus μ-Low J558L cells. Low affinity BCRs were slower to come into molecular proximity and gain FRET, gained less FRET, and, interestingly, lost the gained FRET at a significantly slower rate, indicating that the open conformation was achieved at a slower rate compared with high affinity BCRs. Correlated with enhanced oligomerization and enhanced opening of the BCR was the enhanced recruitment of Syk to the BCR and enhanced calcium responses. Collectively, these results provide a view of a dynamic antigen-driven process in which the conformational changes that ultimately lead to the initiation of signaling are dependent on the affinity of the BCR for antigen such that in high affinity B cells the process is driven forward most efficiently.

In this paper we also explored the antigen affinity dependence of a less well-studied process in the initiation of BCR signaling, namely the growth of BCR microclusters by the recruitment of new BCRs. We determined that microclusters grow dramatically from the time they first form at the initial points of contact of the B cell with an antigen-containing bilayer until they move, in an actin dependent fashion, to form an IS. We studied this process first in the μ-High and μ-Low J558L cells, which we observed did not undergo a characteristic BCR-triggered spreading and contraction response, likely because of the limited signaling ability of these cells. Consequently, BCR microclusters were essentially immobile as they grew. We were also able to study this process in splenic B1-8 primary cells that do spread and contract in response to antigen by focusing on the growth of BCR microclusters during the first 40 s after B cells contacted antigen-containing bilayers before spreading. By fitting the FI of the BCRs and antigen through a 2D Gaussian function, we determined that BCRs increase in both size and in FI with time. Because the microclusters themselves were not moving in the μ-High and μ-Low J558L cells, we conclude that the growth of the microcluster is caused by the trapping of mobile BCRs in the microclusters. These results fit well with our recent single-molecule imaging results showing that highly mobile BCRs stop and are immobilized when they enter BCR microclusters (Tolar et al., 2009a).

The trapping of BCRs in microclusters was selective, as MHC class I molecules showed no stable association with the BCR microclusters. However, we did observe MHC class I molecules within BCR microclusters at early times, within the first 20–40 s, after BCR microclusters formed. We speculate that this phenomenon reflects the nonspecific trapping of MHC class I molecules in areas of confinement in the initial points of contact between the B cell and the antigen-containing lipid bilayer. Similarly, we observed a small accumulation of BCRs in the initial contact points of the B cell with lipid bilayers that did not contain antigen. We suggest that the membrane topology of initial contact points may constrain the movement of membrane receptors to small areas. With time, the MHC class I molecules may diffuse out as antigen-bound BCRs continue to be trapped in the microclusters.

More importantly, we determined that the growth of the BCR microclusters was highly affinity dependent and able to discriminate 50-fold differences in antigen-affinity. As compared with low affinity B cells, the BCR microclusters on high affinity B cells grew more rapidly and reached larger maximal sizes. For the μ-High and μ-Low J558L cells, the affinity dependence of microcluster growth was observed in the absence of a variety of coreceptors and integrins that the J558L B cells fail to express, including CD19 (Wienands et al., 1996; Adachi et al., 2001), a coreceptor that Depoil et al. (2008) recently showed was essential for the B cell spreading and contraction response to membrane-associated antigens.

We believe that these are the first observations to correlate the affinity of a BCR with real-time kinetics of the initiation of BCR oligomerization and clustering. These results define an affinity-dependent step in the very earliest events that initiate BCR signaling. These early BCR-intrinsic events in affinity discrimination are presumably amplified by downstream B cell affinity–dependent events such as those described by Fleire et al. (2006) involving antigen capture during a spreading response. Collectively, these mechanisms allow high affinity B cell clones to compete with lower affinity B cell clones for antigen, T cell help, and survival niches.

MATERIALS AND METHODS

Preparation of fluid planar lipid bilayers. Planar fluid lipid bilayers were prepared as previously described (Brian and McConnell, 1984; Grakoui et al., 1999; Carrasco et al., 2004). In brief, Ni-NTA–containing lipid bilayers were prepared using 1,2-dioleoyl-sn-glycero-3-phosphocholine (DOPC) and 1,2-dioleoyl-sn-glycero-3-[N(5-amino-1-carboxypentyl) iminodiacetic acid]-succinyl (nickel salt; DOGS–Ni-NTA; Avanti Polar Lipids, Inc.) in a 9:1 DOPC/DOGS–Ni-NTA ratio. Unilamellar vesicles were formed by sonication of the mixed lipids and clarified by ultracentrifugation and filtering. Glass coverslips were cleaned by Nanostrip (Cyantek), washed, and dried. Lipid bilayers were prepared from 0.1-mM lipid unilamellar vesicle solutions on the coverslip attached to the bottom of Labtek chambers (Thermo Fisher Scientific).

NIP or pNP conjugated to the peptide ASTGKTASACTSGAS-STGSHis12 (NIP1-His12 or pNP1-His12) and NIP1-His12 and pNP1-His12 coupled to Hylight647 through the cysteine residue were purchased from Anaspec. The hapten–peptide conjugates were HPLC purified and verified by mass spectroscopy with >95% purity. The hapten-coupled peptides were attached to the Ni-NTA–containing lipid bilayer by incubating haptenated peptides (10 or 50 nM) with the bilayer for 20 min at room temperature (RT). Where indicated in the figures, mouse ICAM-1/huFc chimera protein with a 10-nM His12 tag (R&D Systems) was also attached to the lipid bilayers. After washing, the antigen-containing lipid bilayers were used in TIRF imaging. The amount of antigen bound to the bilayer was quantified by titration of the Hylight647-conjugated peptides to resolve

single molecules. The concentration of the peptide attached to the bilayer was calculated by a function of

$$C = N \times D,$$

where C is the concentration (number of molecules per square micrometer), N is the number of Hylight647-conjugated peptide molecules counted at a single-molecule resolution per square micrometer, and D is the titration rate. In our experimental system, incubating bilayers with a 10-nM haptenated peptide solution resulted in bilayers containing ~25 molecules/μm^2, and incubating with a 50-nM solution resulted in a bilayer containing 100 molecules/μm^2 in the planar lipid bilayer.

Mice, cells, antibodies, plasmids, and transfections. B1-8 primary B cells were isolated from the spleens of $IgH^{B1\text{-}8/B1\text{-}8}$ $Ig\kappa^{-/-}$ transgenic mice (provided by M. Shlomchik, Yale University, New Haven, CT) by negative selection using MACS, as previously described (Tolar et al., 2009a). Cy3-conjugated Fab goat antibodies specific for mouse IgM constant regions were purchased from Jackson ImmunoResearch Laboratories, Inc. Antibodies were conjugated with Alexa Fluor 568 using Alexa Fluor mAb labeling kits (Invitrogen) according to the manufacturer's protocols.

A plasmid expressing Igα-YFP was constructed as previously described (Sohn et al., 2008). A plasmid expressing μ-B1-8-CFP fused with a C-terminal CFP through the linker peptide, GGGAAS, was constructed as previously described (Tolar et al., 2005). Using the μ-B1-8-CFP plasmid as a template, μ-B1-8-High-CFP and μ-B1-8-Low-CFP plasmids were generated using a QuikChange II XL Site-Directed Mutagenesis Kit (Agilent Technologies). In mutagenesis PCR, μ-B1-8-High mIgM was generated by mutation of *TGG* to *TTG* (W33L), and μ-B1-8-Low mIgM was generated by mutation of *GCT* to *GGT* (A24G), *AGC* to *ACC* (S31T), *CAC* to *CAG* (H35Q), and *AGA* to *ACT* (R98T). J558L B cell lines expressing the FRET pair of Igα-YFP and μ-B1-8-High-CFP or μ-B1-8-Low-CFP were generated as previously described (Tolar et al., 2005). In brief, a J558L B cell line stably expressing Igα-YFP was first acquired by electroporation, zeocyn selection, and cell sorting. pCDNA3.1-hygromycin plasmids containing μ-B1-8-High-CFP or μ-B1-8-Low-CFP were then transfected into the J558L-Igα-YFP cell line by electroporation. J558L B cell lines stably expressing comparable levels of surface μ-High and μ-Low BCRs were acquired by hygromycin selection and multiple rounds of cell sorting.

Two-color time-lapse live-cell imaging by TIRFM. TIRF images were acquired and analyzed as previously described using a microscope (IX-81; Olympus) equipped with a TIRF port, a 512 × 512 pixel electron-multiplying charge-coupled device (CCD) camera (CascadeII; Roper Industries), and 100× 1.45 NA (Olympus) and 100× 1.4 NA (Carl Zeiss, Inc.) objective lenses. A 442-nm diode pump solid-state laser, a 488-/514-nm argon gas laser, and a 568-/647-nm red krypton/argon gas laser were equipped and used as indicated in the figures. All images were acquired at 37°C on a heated stage. The acquisition was controlled by Metamorph (MDS Analytical Technologies) and the exposure time was 100 ms unless otherwise indicated in the figures. The acquired images were generally analyzed and processed with Image Pro Plus (Media Cybernetics), ImageJ (available at http://rsbweb.nih.gov/ij/), or Matlab (Mathworks) software depending on needs, as indicated in the following paragraphs. Before analysis, images were split, aligned, background subtracted, and corrected for spectral bleed-through using either Image Pro Plus or Matlab software.

B cell microclusters were characterized as previously described (Depoil et al., 2008). In brief, the B cells were labeled with Alexa Fluor 568–Fab anti-IgM, washed twice, and placed on lipid bilayers. Immediately after placing B cells in the chamber, two-color TIRF images were acquired every 2 s using the multiple dimensional acquisition mode controlled by the Metamorph system. For μ-High and μ-Low J558L cells, Igα-YFP and Alexa Fluor 568–Fab anti-IgM were excited by 488- and 568-nm lasers, respectively, and the switch from the 488- to the 568-nm laser was completed by an acoustooptical tunable filter. YFP and Alexa Fluor 568 emission fluorescences were collected by 550/40 ET/BP and 605/40 BP emission filters, respectively, through a 488/568/647 dichroic wheel filter cube. Two-color TIRF images of Igα-YFP and Cy3–Fab anti–MHC I were acquired by staining the cells with Cy3–Fab anti–MHC I. Cy3–Fab anti–MHC I was excited by a 568-nm laser, and Cy3 emission fluorescence was collected by a 605/40 BP emission filter. Similarly, two-color TIRF images of Igα-YFP with either NIP1-His12-Hylight647 or pNP1-His12-Hylight647 were acquired by exciting Hylight647 using a 647-nm laser and collecting Hylight647 emission fluorescence through a 665 LP emission filter. In the case of B1-8 primary B cells, the BCR was labeled by Alexa Fluor 488–Fab anti-IgM.

Recruitment of pSyk into the contact area of the μ-High or μ-Low J558L or B1-8 primary B cells with lipid bilayers was examined by TIRFM after intracellular staining using phospho-ZAP70 (pY319)–Syk (pY352; Cell Signaling Technology and New England Biolabs, Inc., respectively) as previously described (Depoil et al., 2008). In brief, B cells were fixed 10 min after placing on antigen-containing lipid bilayers, permeabilized with 0.1% Triton X-100 in PBS, pretreated with blocking buffer, and stained with phospho-ZAP70 (pY319)–Syk (pY352), followed by Alexa Fluor 647–conjugated $F(ab')_2$ goat antibodies specific for rabbit IgG (Invitrogen). The BCR contact area, the mean FI of BCR, and the numbers of the pSyk microclusters within the contact area were measured and counted using ImageJ software.

FRET image acquisition and FRET efficiency calculation. The acquisition of CFP, FRET, and YFP images by TIRFM and the calculation of FRET efficiency were performed based on previously published protocols, with modifications (Tolar et al., 2005; Sohn et al., 2006, 2008). In brief, a 442-nm laser (CVI Melles Griot) was used to excite CFP and a 514-nm argon gas laser was used to excite YFP in time-lapse TIRF FRET live-cell imaging. CFP, FRET, and YFP TIRF images were acquired every 2 s using the multiple dimensional acquisition mode controlled by the Metamorph system, and the switch of 442- and 514-nm lasers was completed by an acoustooptical tunable filter. CFP and FRET images were acquired by collecting the emission fluorescence using HQ485/30 (CFP) and 550/40 ET/BP emission filters, respectively (Chroma Technology Corp.) with 442-nm laser illumination, and YFP images were acquired by collecting the emission fluorescence using 550/40 ET/BP emission filters with 514-nm laser illumination through a 442/514 dichroic wheel filter cube.

TIRF images were captured into 16-bit grayscale 512 × 512 pixel images without binning and averaging through a CascadeII electron-multiplying CCD camera. FRET efficiency between Igα-YFP and μ-CFP within the BCR complex, in which the stoichiometry of the donor and acceptor is constant, was calculated based on the following equation, as reported in our recent studies (Sohn et al., 2008):

$$FRET = (F/D - \beta - K_D/n/K_A)/(F/D - \beta + K_D).$$

F and D are the mean FI within the region of interest of FRET and CFP TIRF images, respectively, and n is the CFP/YFP stoichiometry, where $n = 2$ in our TIRF FRET experimental system, as reported in our recent studies (Tolar et al., 2005; Sohn et al., 2008). K_A is the ratio of the extinction coefficient of donor (ε_{CFP}) and acceptor (ε_{YFP}) when excited at a donor excitation wavelength of 442 nm. K_D is the result of ratio 1 multiplied by ratio 2, where ratio 1 is the quantum yield of acceptor (Q_{YFP}) divided by donor (Q_{CFP}) and ratio 2 is a constant F (C_F) divided by a constant D (C_D). C_F is a constant defining the efficiency of detection acceptor FI with the TIRF FRET filter setup, and C_D is a constant defining the efficiency of donor FI with the TIRF CFP filter setup. In our experimental system, K_A and K_D were calculated based on the following equations, as reported previously (Tolar et al., 2005; Sohn et al., 2006, 2008):

$$K_A = (F - \beta \times D - \gamma \times A)/(\gamma \times A \times E_{bleaching})$$

$$K_D = (F - \beta \times D - \gamma \times A)/(D \times E_{bleaching}) - (F - \beta \times D - \gamma \times A)/D$$

$$E_{bleaching} = (1 - D_{before}/D_{after}).$$

D_{before} and D_{after} values were, respectively, the donor CFP mean FI in CFP channel before and after complete photobleaching of acceptor YFP. To calculate the D_{before} and D_{after}, we used Daudi human B cells expressing a Lyn16-CFP-YFP fusion protein, a construct with a 1:1 CFP/YFP ratio and a fixed distance between CFP and YFP proteins producing positive FRET efficiency, as previously reported (Tolar et al., 2005; Sohn et al., 2006, 2008). A is the mean FI within the region of interest of YFP TIRF images. In the previously described equations, β and γ were, respectively, the correction factors for donor (CFP) bleed-through (β) in the FRET channel and acceptor (YFP) cross talk (γ) in the FRET channel. In this study, both the β and γ values were calculated from TIRF images of a single CFP- or YFP-expressing CH27 B cell acquired using the same TIRFM settings as for the experimental cells. In our TIRFM settings, the bleed-through of YFP emission to the CFP channel (δ) from the YFP single-positive cell was negligible and, thus, was counted as zero in the calculation of FRET efficiency.

The processing of TIRF FRET images was analyzed mainly using an Image Pro Plus software package according to previously described protocols (Tolar et al., 2005; Sohn et al., 2006, 2008). In brief, CFP, FRET, and YFP images were background subtracted and smoothed by a Gauss filter. For the quantification of FRET efficiency at the single-cell level with time, the mean FI from the TIRF images of CFP (D), FRET (F), and YFP (A) were acquired by the autotracking function of Image Pro Plus software. When tracking, the contact area of the cell as a whole was taken as the region of interest, and the 3 × 3 pixel autotracking mode was used in the software setup. The background FI in close proximity to BCR microclusters was used as the lower-end threshold in the segmentation setup of the autotracking mode.

In this study, FRET efficiency was given as the mean ± SD or ΔFRET ± SD as specified in the figures, where ΔFRET is the maximal change of FRET efficiency compared with the initial FRET value throughout the entire time course of imaging. Kinetics of the FRET-efficient losing plot were fitted exclusively by setting the plateau FRET efficiency as 100% before losing starts in both μ-High and μ-Low J558L cells, and the following exponential decay function was used to acquire τ_{50}, where t is the independent variable and τ_{50} is the fit coefficient:

$$f(t) = A \times \exp(-t / \tau_{50}).$$

Single-particle tracking and analysis. In single-molecule TIRF imaging, μ-High or μ-Low J558L cells or B1-8 primary B cells were labeled with 1 nM of Fab Alexa Fluor 568–conjugated anti-IgM antibodies for the best resolution of individual fluorescence spots without the need for further extensive photobleaching, as previously reported (Tolar et al., 2009a). Labeled B cells were washed twice before incubation with antigen-containing lipid bilayers, and images were taken using TIRFM with a 568-nm laser at an output power of 2.5 mW at the objective lens in epifluorescence mode. A 605/40 BP emission filter was used for collection of Alexa Fluor 568 fluorescence. A subregion of roughly 100 × 100 pixels of the available area of the electron-multiplying CCD chip (512 × 512 pixels) was used to achieve an exposure time of 35 ms per frame. A single-molecule BCR was captured on 300 frames in a time course of 10 s in streamline acquisition mode, the time resolution of which was found to be sufficient to reliably track the single-molecule BCRs, as previously reported (Tolar et al., 2009a).

Analysis of single-molecule tracking results was performed as described in our previous study (Tolar et al., 2009a). Single-molecule tracking was performed using Matlab code based on available positional fitting and tracking algorithms (Crocker and Grier, 1996; Douglass and Vale, 2005, 2008). The resulting trajectories were visually inspected and occasional errors in tracking were manually corrected. MSD and short-range diffusion coefficients for each BCR molecule trajectory (D_0, based on time intervals of 35–140 ms) were calculated from positional coordinates, as previously reported (Douglass and Vale, 2005, 2008), and plotted as CPD graphs. In this study, thousands of single-molecule BCR trajectories from at least 12 cells were acquired and analyzed for each condition in each experiment, as detailed in the figure legends. The MSD plot was mathematically fitted into a confined diffusion model by the following monoexponential function to acquire the size of the confinement microdomain L, where t is the independent variable and L and D_0 are the fitting coefficients:

$$f(t) = a + \frac{L^2}{3}\left(1 - e^{-\frac{12D_0 t}{L^2}}\right).$$

Analysis of intensities and sizes of BCR and antigen microclusters. Precise 2D positions and integrated FIs of the BCR or antigen microclusters in time-lapse TIRF images were obtained by means of least square fitting of a 2D Gaussian function to each of the 2D FI profiles. Because some of the profiles were found not to be perfectly circular, the Gaussian function was allowed to adopt an elliptical shape (Holtzer et al., 2007),

$$f(x,y) = z_0 + I\frac{41n2}{\pi\sigma_r^2} e^{-\left[41n2\left(\frac{(x-x_c)^2}{\sigma_r^2/\varepsilon^2} + \frac{(y-y_c)^2}{\sigma_r^2\varepsilon^2}\right)\right]},$$

in which the ellipticiy is defined as

$$\varepsilon = \sqrt{\sigma_y / \sigma_x},$$

and a generalized 2D width as

$$\sigma_r^2 = \sqrt{\sigma_x^2 \sigma_y^2}.$$

For each microcluster, the fit yields the parameter's local background FI (z_0), position (x_c, y_c), integrated FI, and generalized FWHM (σ_x, σ_y) of the intensity distribution in the x and y direction, respectively (Fig. S4 A).

Only microclusters that were successfully tracked for at least 10 steps and only the first 60 steps (120 s) of each track of the BCR microclusters from μ-High and μ-Low J558L cells or only the first 20 steps (40 s) of each track from B1-8 primary B cell microclusters were selected for analysis. This selection was necessary to avoid tracking and Gaussian fitting errors, both of which arise from spots merging and overlapping at later stages of the observed processes. If two spots merge, tracking for one of them is inevitably terminated, whereas Gaussian fitting is only reliable on well-separated and approximately round spots. For the intensity and size analyses, arithmetic means and standard errors of the values of the respective parameters were calculated for all selected spots present in one frame and plotted versus time. Finally, values belonging to the same track were normalized to the first position of the track. The statistical test used to compare the kinetics of microcluster growth is as previously described (Elso et al., 2004; Baldwin et al., 2007) or through the online server available at http://bioinf.wehi.edu.au/software/compareCurves/index.html.

Measurements of calcium influx from B cells on a planar lipid bilayer. For measurement of intracellular calcium influx in B cells stimulated by membrane-associated antigen, B1-8 primary B cells were incubated with 2 μg/ml Fluor-4AM and 5 μg/ml FuraRed-AM in the presence of 4 mM probenecid (Invitrogen). Cells were illuminated with epifluorescence immediately after placing on the lipid bilayers, and calcium concentrations were expressed as ratios of Fluo4 to FuraRed FI.

Treatment of B cells with pharmaceutical inhibitors. For inhibitor studies, μ-High J558L cells were successively pretreated with specific inhibitors at the temperature and for the time course indicated in the figures before imaging, as previously reported (Tolar et al., 2005; Sohn et al., 2006, 2008). In brief, the μ-High J558L cells were pretreated with 50 μM of the Src family tyrosine kinase inhibitor PP2 for 10 min at RT to inhibit BCR signaling, or were pretreated with 50 μM piceatannol for 10 min at RT to block the specific phosphorylation of the Syk substrate BLNK in the early BCR signaling pathway (Tolar et al., 2005). The μ-High J558L cells were pretreated with

100 μM monodansylcadaverine for 10 min at RT to block internalization, or were pretreated with 1 μM latrunculin B for 10 min at RT to block actin polymerization (Tolar et al., 2005). The μ-High J558L cells were pretreated with 1 μM jasplakinolide for 45 min at 37°C to block actin depolymerization (Bubb et al., 2000), or were pretreated with 2 μM nocodazole for 1 h at 4°C followed with another 0.5 h at 37°C, a procedure to efficiently disrupt the tubulin-cytoskeleton filaments (Schliwa and Euteneuer, 1978; Rodionov et al., 2003). The μ-High J558L cells were pretreated for 30 min at RT with 100 μM colchicine to disrupt microtubule filaments or 100 μM taxol to stabilize microtubule filaments (Huby et al., 1998). As a control, the μ-High J558L cells were pretreated with DMSO for 1 h at 4°C, followed with another 0.5 h at 37°C before imaging.

Surface plasmon resonant binding assay. To acquire the affinity constant K_A of various B1-8 antibodies with either NIP- or pNP-hapten antigen peptide, the real-time binding kinetics of B1-8 antibodies at five different concentrations with the immobilized peptide antigen on biosensor chips (CM5; BIAcore AB) were examined by a surface plasmon resonance instrument (model 3000; BIAcore AB). NIP1-His12 or pNP-His12 peptide antigens were immobilized on sensor chips using an amine-coupling procedure according to the manufacture's protocols. In brief, the dextran layer of the sensor surface was activated by a fresh mixture of N-ethyl-N′-(3-dimethylaminopropyl) carbodiimide hydrochloride and N-hydroxysuccinimide (BIAcore AB). NIP1-His12 or pNP-His12 peptide antigens were injected and coupled to the chip surface. The chip was then blocked by ethanolamine for the remaining active surface (BIAcore AB). B1-8 or B1-8-High antibodies were provided by G. Kelsoe (Duke University, Durham, NC).

To acquire B1-8-Low antibodies, point mutants of *CAACTG* to *TAATAG* were made in the cDNA of membrane-version γ-B1-8-Low mIgG to introduce a stop codon immediately after the mIgG extracellular proximal membrane amino acid sequence SHSPGL using a QuikChange II XL Site-Directed Mutagenesis Kit. The underlined nucleotides indicate where the mutations were introduced for stop codons in Mutagenesis PCR. The acquired soluble version of γ-B1-8-Low IgG (γ-B1-8-Low sIgG) cDNA was transfected by electroporation into J558L B cells expressing an endogenous Igλ1 light chain. The derivative J558L B cell lines stably expressing soluble B1-8-Low antibodies (J558L-solule-B1-8-Low) were acquired by hygromycin selection and sandwich ELISA screening. In the sandwich ELISA assay, NIP25-BSA was used as a coating antigen to capture B1-8-Low antibodies in the cell culture of all of the derivative J558L B cell clones after hygromycin selection. B1-8-Low antibodies were purified using a protein A column from 500 ml of serum-free J558L-solule-B1-8-Low B cell culture supernatant.

Five different concentrations of B1-8-Low, B1-8, or B1-8-High antibodies, as indicated in figure legends, were flowed through and measured for the real-time association and dissociation kinetics with either NIP1-His12 or pNP1-His12 hapten antigens immobilized on chip surfaces. The kinetic association and dissociation curves of each antibody–antigen pair were fitted to BIAevaluation software (BIAcore) to calculate the affinity constant K_A, on-rate $K_{forward}$, and off-rate K_{back} for each antigen–antibody pair.

Online supplemental material. Fig. S1 shows the real-time association and dissociation kinetics for the binding of B1-8 antibodies to NIP1 or pNP1 conjugated to the peptide His12 by BIAcore surface plasmon resonance. Fig. S2 shows the surface expression of BCRs on μ-High and μ-Low J558L cells and schematically presents the experimental design of two-color live-cell time-lapse imaging in TIRFM. Fig. S3 shows that the growth of BCR microclusters is selective and excludes MHC class I molecules. Fig. S4 schematically presents the 2D Gaussian spreading function used in this report for the mathematical fittings of the microclusters, and three additional Gaussian functions in different perspectives are shown to illustrate their visual appearance with respect to variations in integrated FI and FWHM. Fig. S5 demonstrates that the growth of BCR microclusters is antigen affinity dependent. Fig. S6 shows the accumulation of BCRs and antigen into microclusters in B1-8 primary B cells placed on NIP1-His12-Hylight647–containing lipid bilayers. Fig. S7 shows that B1-8 primary B cells activated by the membrane-bound high affinity antigen NIP1-His12 show faster and stronger calcium responses compared with B cells activated by the low affinity antigen pNP1-His12. Video 1 shows that high affinity BCRs are enhanced in their ability to form immobile oligomers. Videos 2–4 show that the accumulation of BCRs and antigens into the contact area between B cells and antigen-containing planar lipid bilayers is affinity dependent. Video 5 shows that BCR microclusters grow in FI with time when encountering antigen-containing lipid bilayers. Video 6 shows that antigen microclusters grow with time when encountering antigen-containing lipid bilayers. Video 7 shows that the growth of BCR microclusters is selective. Video 8 shows that the growth of BCR microclusters is antigen affinity dependent. Video 9 shows that the BCR and antigen microclusters in B1-8 primary B cells grow as they are moved into the center B cell synapse. Video 10 shows that the B1-8 primary B cells activated by the membrane-bound high affinity antigen NIP1-His12 show faster and stronger calcium responses as compared with cells activated by the low affinity antigen pNP1-His12. Online supplemental material is available at http://www.jem.org/cgi/content/full/jem.20092123/DC1.

We thank Dr. G. Kelsoe and Dr. R. Brink (Garvan Institute of Medical Research, Sydney, Australia) for their helpful suggestions and for providing experimental materials, and, as always, Dr. J. Brzostowski for expert advice on imaging.

This work has been supported by the Intramural Research Program of the National Institute of Allergy and Infectious Diseases, National Institutes of Health.

The authors have no conflicting financial interests.

Submitted: 1 October 2009
Accepted: 11 March 2010

REFERENCES

Adachi, T., J. Wienands, C. Wakabayashi, H. Yakura, M. Reth, and T. Tsubata. 2001. SHP-1 requires inhibitory co-receptors to down-modulate B cell antigen receptor-mediated phosphorylation of cellular substrates. *J. Biol. Chem.* 276:26648–26655. doi:10.1074/jbc.M100997200

Allen, D., T. Simon, F. Sablitzky, K. Rajewsky, and A. Cumano. 1988. Antibody engineering for the analysis of affinity maturation of an anti-hapten response. *EMBO J.* 7:1995–2001.

Baldwin, T., A. Sakthianandeswaren, J.M. Curtis, B. Kumar, G.K. Smyth, S.J. Foote, and E. Handman. 2007. Wound healing response is a major contributor to the severity of cutaneous leishmaniasis in the ear model of infection. *Parasite Immunol.* 29:501–513. doi:10.1111/j.1365-3024.2007.00969.x

Batista, F.D., and N.E. Harwood. 2009. The who, how and where of antigen presentation to B cells. *Nat. Rev. Immunol.* 9:15–27. doi:10.1038/nri2454

Berek, C., G.M. Griffiths, and C. Milstein. 1985. Molecular events during maturation of the immune response to oxazolone. *Nature.* 316:412–418. doi:10.1038/316412a0

Brian, A.A., and H.M. McConnell. 1984. Allogeneic stimulation of cytotoxic T cells by supported planar membranes. *Proc. Natl. Acad. Sci. USA.* 81:6159–6163. doi:10.1073/pnas.81.19.6159

Brink, R., T.G. Phan, D. Paus, and T.D. Chan. 2008. Visualizing the effects of antigen affinity on T-dependent B-cell differentiation. *Immunol. Cell Biol.* 86:31–39. doi:10.1038/sj.icb.7100143

Bubb, M.R., I. Spector, B.B. Beyer, and K.M. Fosen. 2000. Effects of jasplakinolide on the kinetics of actin polymerization. An explanation for certain in vivo observations. *J. Biol. Chem.* 275:5163–5170. doi:10.1074/jbc.275.7.5163

Carrasco, Y.R., and F.D. Batista. 2006. B cell recognition of membrane-bound antigen: an exquisite way of sensing ligands. *Curr. Opin. Immunol.* 18:286–291. doi:10.1016/j.coi.2006.03.013

Carrasco, Y.R., and F.D. Batista. 2007. B cells acquire particulate antigen in a macrophage-rich area at the boundary between the follicle and the subcapsular sinus of the lymph node. *Immunity.* 27:160–171. doi:10.1016/j.immuni.2007.06.007

Carrasco, Y.R., S.J. Fleire, T. Cameron, M.L. Dustin, and F.D. Batista. 2004. LFA-1/ICAM-1 interaction lowers the threshold of B cell activation by

facilitating B cell adhesion and synapse formation. *Immunity*. 20:589–599. doi:10.1016/S1074-7613(04)00105-0

Crocker, J.C., and D.G. Grier. 1996. Methods of digital video microscopy for colloidal studies. *J. Colloid Interface Sci.* 179:298–310. doi:10.1006/jcis.1996.0217

Dal Porto, J.M., A.M. Haberman, G. Kelsoe, and M.J. Shlomchik. 2002. Very low affinity B cells form germinal centers, become memory B cells, and participate in secondary immune responses when higher affinity competition is reduced. *J. Exp. Med.* 195:1215–1221. doi:10.1084/jem.20011550

Depoil, D., S. Fleire, B.L. Treanor, M. Weber, N.E. Harwood, K.L. Marchbank, V.L. Tybulewicz, and F.D. Batista. 2008. CD19 is essential for B cell activation by promoting B cell receptor-antigen microcluster formation in response to membrane-bound ligand. *Nat. Immunol.* 9:63–72. doi:10.1038/ni1547

Douglass, A.D., and R.D. Vale. 2005. Single-molecule microscopy reveals plasma membrane microdomains created by protein-protein networks that exclude or trap signaling molecules in T cells. *Cell*. 121:937–950. doi:10.1016/j.cell.2005.04.009

Douglass, A.D., and R.D. Vale. 2008. Single-molecule imaging of fluorescent proteins. *Methods Cell Biol.* 85:113–125. doi:10.1016/S0091-679X(08)85006-6

Elso, C.M., L.J. Roberts, G.K. Smyth, R.J. Thomson, T.M. Baldwin, S.J. Foote, and E. Handman. 2004. Leishmaniasis host response loci (lmr1-3) modify disease severity through a Th1/Th2-independent pathway. *Genes Immun.* 5:93–100. doi:10.1038/sj.gene.6364042

Fleire, S.J., J.P. Goldman, Y.R. Carrasco, M. Weber, D. Bray, and F.D. Batista. 2006. B cell ligand discrimination through a spreading and contraction response. *Science*. 312:738–741. doi:10.1126/science.1123940

Foote, J., and C. Milstein. 1991. Kinetic maturation of an immune response. *Nature*. 352:530–532. doi:10.1038/352530a0

Grakoui, A., S.K. Bromley, C. Sumen, M.M. Davis, A.S. Shaw, P.M. Allen, and M.L. Dustin. 1999. The immunological synapse: a molecular machine controlling T cell activation. *Science*. 285:221–227. doi:10.1126/science.285.5425.221

Griffiths, G.M., C. Berek, M. Kaartinen, and C. Milstein. 1984. Somatic mutation and the maturation of immune response to 2-phenyl oxazolone. *Nature*. 312:271–275. doi:10.1038/312271a0

Harwood, N.E., and F.D. Batista. 2008. New insights into the early molecular events underlying B cell activation. *Immunity*. 28:609–619. doi:10.1016/j.immuni.2008.04.007

Holtzer, L., T. Meckel, and T. Schmidt. 2007. Nanometric three-dimensional tracking of individual quantum dots in cells. *Appl. Phys. Lett.* 90:053902. doi:10.1063/1.2437066

Huby, R.D., A. Weiss, and S.C. Ley. 1998. Nocodazole inhibits signal transduction by the T cell antigen receptor. *J. Biol. Chem.* 273:12024–12031. doi:10.1074/jbc.273.20.12024

Junt, T., E.A. Moseman, M. Iannacone, S. Massberg, P.A. Lang, M. Boes, K. Fink, S.E. Henrickson, D.M. Shayakhmetov, N.C. Di Paolo, et al. 2007. Subcapsular sinus macrophages in lymph nodes clear lymph-borne viruses and present them to antiviral B cells. *Nature*. 450:110–114. doi:10.1038/nature06287

Kouskoff, V., S. Famiglietti, G. Lacaud, P. Lang, J.E. Rider, B.K. Kay, J.C. Cambier, and D. Nemazee. 1998. Antigens varying in affinity for the B cell receptor induce differential B lymphocyte responses. *J. Exp. Med.* 188:1453–1464. doi:10.1084/jem.188.8.1453

McHeyzer-Williams, L.J., and M.G. McHeyzer-Williams. 2005. Antigen-specific memory B cell development. *Annu. Rev. Immunol.* 23:487–513. doi:10.1146/annurev.immunol.23.021704.115732

Milstein, C. 1991. Affinity maturation of antibodies. *Immunol. Today*. 12:93–94. doi:10.1016/0167-5699(91)90164-O

Pape, K.A., D.M. Catron, A.A. Itano, and M.K. Jenkins. 2007. The humoral immune response is initiated in lymph nodes by B cells that acquire soluble antigen directly in the follicles. *Immunity*. 26:491–502. doi:10.1016/j.immuni.2007.02.011

Paus, D., T.G. Phan, T.D. Chan, S. Gardam, A. Basten, and R. Brink. 2006. Antigen recognition strength regulates the choice between extrafollicular plasma cell and germinal center B cell differentiation. *J. Exp. Med.* 203:1081–1091. doi:10.1084/jem.20060087

Phan, T.G., D. Paus, T.D. Chan, M.L. Turner, S.L. Nutt, A. Basten, and R. Brink. 2006. High affinity germinal center B cells are actively selected into the plasma cell compartment. *J. Exp. Med.* 203:2419–2424. doi:10.1084/jem.20061254

Phan, T.G., I. Grigorova, T. Okada, and J.G. Cyster. 2007. Subcapsular encounter and complement-dependent transport of immune complexes by lymph node B cells. *Nat. Immunol.* 8:992–1000. doi:10.1038/ni1494

Qi, H., J.G. Egen, A.Y. Huang, and R.N. Germain. 2006. Extrafollicular activation of lymph node B cells by antigen-bearing dendritic cells. *Science*. 312:1672–1676. doi:10.1126/science.1125703

Rodionov, V., J. Yi, A. Kashina, A. Oladipo, and S.P. Gross. 2003. Switching between microtubule- and actin-based transport systems in melanophores is controlled by cAMP levels. *Curr. Biol.* 13:1837–1847.

Schliwa, M., and U. Euteneuer. 1978. A microtuble-independent component may be involved in granule transport in pigment cells. *Nature*. 273:556–558. doi:10.1038/273556a0

Shih, T.A., E. Meffre, M. Roederer, and M.C. Nussenzweig. 2002a. Role of BCR affinity in T cell dependent antibody responses in vivo. *Nat. Immunol.* 3:570–575. doi:10.1038/ni803

Shih, T.A., M. Roederer, and M.C. Nussenzweig. 2002b. Role of antigen receptor affinity in T cell-independent antibody responses in vivo. *Nat. Immunol.* 3:399–406. doi:10.1038/ni776

Sohn, H.W., P. Tolar, T. Jin, and S.K. Pierce. 2006. Fluorescence resonance energy transfer in living cells reveals dynamic membrane changes in the initiation of B cell signaling. *Proc. Natl. Acad. Sci. USA*. 103:8143–8148. doi:10.1073/pnas.0509858103

Sohn, H.W., P. Tolar, and S.K. Pierce. 2008. Membrane heterogeneities in the formation of B cell receptor–Lyn kinase microclusters and the immune synapse. *J. Cell Biol.* 182:367–379. doi:10.1083/jcb.200802007

Takahashi, Y., P.R. Dutta, D.M. Cerasoli, and G. Kelsoe. 1998. In situ studies of the primary immune response to (4-hydroxy-3-nitrophenyl)acetyl. V. Affinity maturation develops in two stages of clonal selection. *J. Exp. Med.* 187:885–895. doi:10.1084/jem.187.6.885

Tolar, P., and S.K. Pierce. 2010. A conformation-induced oligomerization model for B cell receptor microclustering and signaling. *Curr. Top. Microbiol. Immunol.* 340:155–169. doi:10.1007/978-3-642-03858-7_8

Tolar, P., H.W. Sohn, and S.K. Pierce. 2005. The initiation of antigen-induced B cell antigen receptor signaling viewed in living cells by fluorescence resonance energy transfer. *Nat. Immunol.* 6:1168–1176. doi:10.1038/ni1262

Tolar, P., H.W. Sohn, and S.K. Pierce. 2008. Viewing the antigen-induced initiation of B-cell activation in living cells. *Immunol. Rev.* 221:64–76. doi:10.1111/j.1600-065X.2008.00583.x

Tolar, P., J. Hanna, P.D. Krueger, and S.K. Pierce. 2009a. The constant region of the membrane immunoglobulin mediates B cell-receptor clustering and signaling in response to membrane antigens. *Immunity*. 30:44–55. doi:10.1016/j.immuni.2008.11.007

Tolar, P., H.W. Sohn, W. Liu, and S.K. Pierce. 2009b. The molecular assembly and organization of signaling active B-cell receptor oligomers. *Immunol. Rev.* 232:34–41. doi:10.1111/j.1600-065X.2009.00833.x

Wienands, J., O. Larbolette, and M. Reth. 1996. Evidence for a preformed transducer complex organized by the B cell antigen receptor. *Proc. Natl. Acad. Sci. USA*. 93:7865–7870. doi:10.1073/pnas.93.15.7865